https://doi.org/10.5194/egusphere-2026-3737
Preprint. Discussion started: 28 August 2026

The Cloud-Aerosol Transition Zone Derived from Ground-Based and Satellite Lidars

Jaume Ruiz de Morales[1], Josep Calbó[1], Josep-Abel González[1], Hendrik Andersen[2,3], Jan Cermak[2,3], Julia Fuchs[2,3], Yolanda Sola[4], José Luis Gómez-Amo[5]

[1]Departament de Física, Universitat de Girona, Girona, Spain
[2]Institute of Meteorology and Climate Research, Karlsruhe Institute of Technology (KIT), Karlsruhe, Germany
[3]Institute of Photogrammetry and Remote Sensing, Karlsruhe Institute of Technology (KIT), Karlsruhe, Germany
[4]Departament de Física Aplicada – Meteorologia, Universitat de Barcelona, Barcelona, Spain
[5]Departament de Física de la Terra i Termodinàmica, Universitat de València, Burjassot, Spain

Correspondence to: Jaume Ruiz de Morales (jaume.ruizdemorales@udg.edu)

Abstract. The contribution of Aerosol-Cloud Interactions (ACI) to the Earth's radiative budget remains a major source of uncertainty in future climate projections. Clouds continuously interact with the surrounding non-saturated environment, forming cloud-aerosol transition zones (TZs). The suspensions in these regions are not fully assessed by cloud-cloudless distinction methodologies and have a non-negligible role in the Earth's radiative budget, making the lack of large-scale TZ observations a challenge for full comprehension of the climate system. This study assesses TZ distributions using ground-based and spaceborne lidar observations to improve understanding of TZ conditions and evaluate the respective instrument capabilities. Ground-based Automatic low-power Lidars and Ceilometers (ALC) located at Burjassot (Spain), Gruenow (Germany), Girona (Spain) and the Cloudnet network are used, along with CALIOP observations over the region between 30º–80º N and 10º W–35º E, covering Europe. Results show that cloud-to-clear transitions are gradual, depend on detection thresholds and local climatology. Coincidental ALC and CALIOP observations are presented to assess the potential complementarity between the methods. Overall, ground-based ALCs provide high temporal and vertical resolution and are particularly effective at detecting TZs at low altitudes. In contrast, CALIOP offers global coverage and is especially useful for detecting TZs at high altitudes. Both methods show good agreement for cloud classification. However, there are some differences for aerosol and TZ detections due to instrument capabilities, altitude sensitivity, and the classification techniques. Although each approach has its individual limitations, integrating spaceborne downward-looking and ground-based upward-looking lidar observations provides a more comprehensive characterization of cloud-TZ-aerosol distribution.

1 Introduction

Reliable future climate projections depend on the accuracy to represent the factors that heat and cool the climate system, as well as the processes that influence their environmental response (Masson-Delmotte et al., 2021). Variations in radiative forcing are primarily driven by changes in greenhouse gases (GHGs), atmospheric aerosols, and clouds. While GHGs (e.g. CO_2, CH_4, N_2O, O_3 and halogenated gases) account for the most positive radiative forcing and their contribution is well constrained, limited knowledge of climate forcing by clouds, aerosols, and aerosol-cloud interactions (ACI) constitutes the primary source of uncertainty in overall forcing changes (Boucher et al., 2013, Masson-Delmotte et al., 2021; Chen et al., 2024). Clouds and aerosols affect the Earth's energy budget by absorbing and scattering shortwave (i.e. solar) and longwave (i.e. thermal) radiation. Additionally, clouds and aerosols interact with each other further complicating their assessment. Aerosols can serve as cloud condensation nuclei (CCN), modifying cloud microphysics, radiative properties and lifetime (Twomey et al., 1974, 1991; Albrecht et al., 1989). Conversely, cloud droplets can provide a more humid environment, also known as "moist halo region" (Gu et al., 2024), enhancing aerosol hygroscopic growth processes (Wen et al., 2023). Microphysical processes

https://doi.org/10.5194/egusphere-2026-3737
Preprint. Discussion started: 28 August 2026

vary between different regions of the cloud (Wang et al., 2025a). While the highest supersaturation is reached at the cloud base and within core updraft regions (e.g., Gong et al., 2023), the cloud centres contain a higher supply of water vapor where droplet growth is dominated by collision-coalescence processes. Whereas on cloud edges, as water vapour is limited, droplet growth is dominated by condensation and evaporation processes (Wang et al., 2025a). Thus, aerosol properties near cloud boundaries are different from those in cloud-free environments (Twohy et al., 2009).

Several factors make clouds particularly challenging for climate modelling (Ceppi et al., 2017; Alizadeh et al., 2022; Kahn et al., 2023). Clouds are complex and dynamic, involving feedbacks among thermodynamic, microphysical, and radiative processes that interact across spatial scales ranging from micrometres to hundreds of kilometres (Ronen et al., 2025). As the typical grid size in global climate models (GCMs) is much larger than most individual clouds, and obviously much larger than cloud micro-processes, they are usually represented by simplified sub-grid parametrizations and are not directly resolved (Ronen et al., 2025). Furthermore, clouds interact continuously with the surrounding non-saturated environment, forming atmospheric suspensions with properties that lie between those of 'pure' clouds and 'pure' aerosols, referred to as the cloud-aerosol transition zone (Calbó et al., 2024) or twilight zone (Koren et al., 2007), and here denoted as TZ from now on. The lack of large-scale observational constraints on ACI is another longstanding challenge for representing clouds in GCMs (Ghan et al., 2016; Wang et al., 2025b).

The TZ comprises all atmospheric suspensions that cannot be clearly classified as either cloud or aerosol, such as hydrated aerosols, haze, or forming/evaporating cloud fragments, features that are often overlooked by traditional binary cloud/cloud-free classification methods. Understanding and characterizing the properties of TZ conditions is essential for reducing uncertainties in global radiative forcing (Wen et al., 2024). Recent studies have shown that at the top of the atmosphere (TOA) the TZ longwave radiative effect for shallow clouds is about 0.75 W m^{-2} (Eytan et al., 2020; Jahani et al., 2020, 2022), and when considering all cloud transition zones, including those from high clouds, the longwave radiative effect rises to just above 1 W m^{-2} (Eytan et al., 2025). The TZ shortwave radiative effect is about –9 W m^{-2} near noon, which is larger in absolute terms than the diurnal average radiative effect of aerosols for non-cloudy skies over the oceans, estimated to be less negative than –5 W m^{-2} (Eytan et al., 2025). The TZ conditions are estimated to extend up to 15 km away from clouds (Várnai and Marshak, 2011) and are found ubiquitously over the planet (Várnai and Marshak, 2011; Fuchs et al., 2015; Ruiz de Morales et al., 2026). Over 60% of Earth is covered by clouds (King et al., 2013), while TZ is estimated to affect more than 50% of the cloud-free atmosphere, since half of all cloud-free profiles are closer than 4.4 km to a low-level cloud, and 75% of them are closer than 20 km (Várnai and Marshak, 2011). The TZ frequency of occurrence has been further assessed using several ground-based methods: Calbó et al. (2017) determined that at least 10% of the analyzed period exhibited TZ conditions using sky camera images, and broadband and spectral solar radiation measurements; González et al. (2023) found that 10–15% of downwelling longwave radiation observations could be attributed to the TZ. Other recent studies on TZ conditions are those of Scarlatti et al. (2023, 2024), which used machine-learning approaches from all-sky camera imagery to study aerosol properties, especially in partially cloudy environments.

While most of these studies considered the atmospheric conditions integrated over the entire column, lidar-based studies highlighted the importance of accounting for the TZ vertical distribution, as its structure can affect the interpretation of column integrated measurements. This is a main motivation for the present study. For example, Yang et al. (2024) developed a methodology to observe droplet activation within the cloud base at decimetre scale by using a single-photon lidar, and Ruiz de Morales et al. (2024) showed that when analyzing all layers detected along the vertical with a ground-based ceilometer, TZ conditions are as frequent as cloudy ones. Furthermore, Hu et al. (2025) explored the seasonal changes in hygroscopicity and optical properties of the aerosols beneath low-level clouds, what they termed "a subcloud transition zone (SCTZ)", by using Raman Lidar retrievals, along with meteorological ground-based observations, and radiosonde data. They found that although surface aerosols are more hygroscopic in autumn and winter due to their higher inorganic content, in the SCTZ, hygroscopicity and backscatter are enhanced in summer due to more frequent cloud fragmentation processes at convective cloud bases; there, about 66.7% of the

https://doi.org/10.5194/egusphere-2026-3737
Preprint. Discussion started: 28 August 2026

enhancement is attributed to aerosol hygroscopic growth and 33.3% to cloud fragments. Other studies have also used satellite lidar to study the global distribution and frequency of occurrence of TZ conditions (Várnai and Marshak, 2011; Fuchs et al., 2015; Ruiz de Morales et al., 2026).

Lidar technology is considered as a leading technique to study the atmospheric vertical structure, and more recently for studying ACI (Cairo et al., 2024). Automatic Low Power Lidars and Ceilometers (ALC) are particularly versatile instruments, as their backscatter retrievals can be used to study a wide range of atmospheric phenomena (Rogers et al., 1997; Haeffelin et al., 2016; Kotthaus and Grimmond, 2018; Harrison et al., 2018; Kotthaus et al., 2020; Malik et al., 2025). ALCs are also more cost-effective and widely available (as they are used in airports, weather stations, national meteorological services and research campaigns) than Raman or multiwavelength lidars. As a result, many ALC and lidar networks have been established for atmospheric research, such as the Global Atmospheric Watch (GAW) Aerosol Lidar Observation Network (GALION; Yuba et al., 2023) from the World Meteorological Organization (WMO), the European Aerosol Research Lidar Network (EARLINET; Pappalardo et al., 2014), the E-Profile program from the European Meteorological Network (EUMETNET), the NASA Micro Pulse Lidar Network (MPLNET; Welton et al., 2018), the Asian Dust and Aerosol Lidar Observation Network (AD-Net; Nishizawa et al., 2016), the Latin American Lidar Network (LALINET; Guerrero-Rascado et al., 2016), the Automated Lidar-Ceilometer network (ALICEnet; Bellini et al., 2024), or the Iberian Ceilometer Network (ICENET; Cazorla et al., 2017). Lidar systems have also been used on satellite platforms. A particularly interesting satellite-based lidar for comparison with ground-based profiling data is the Cloud-Aerosol Lidar with Orthogonal Polarization (CALIOP) onboard the Cloud-Aerosol Lidar and Infrared Pathfinder Satellite Observations (CALIPSO) satellite, which has provided over 17 years of unprecedented measurements of the Earth's atmosphere vertical structure. The CALIPSO mission ended in August 2024, and since May 2024 the joint ESA/JAXA EarthCARE mission is succeeding CALIPSO in observing aerosols and clouds with active remote sensing techniques from space (Illingworth et al., 2015; Wehr et al., 2023).

The integration of satellite and ground-based lidar observations has become an increasingly popular research topic, particularly for studying aerosols (Deng et al., 2024a), pollution and smoke (Yang et al., 2022; Fang et al., 2024), dust (Marcos et al., 2016), characteristics of the planetary boundary layer (PBL) (Li et al., 2021; Kim et al., 2021), cloud structures (Kim et al., 2011; Baroni et al., 2020), cirrus clouds (Kim et al., 2014; Deng et al., 2024b), polar stratospheric clouds (Snels et al., 2021) and satellite retrieval validation (Kim et al., 2008; Mamouri et al., 2009; Perrone et al., 2011). Ground-based lidars provide high temporal and spatial resolution information about the vertical structure of atmospheric layers, but their spatial coverage is limited to local or regional scales. In contrast, space-borne lidar observations offer worldwide coverage of the vertical atmospheric distributions, but with lower spatial resolution. Combining both observation methods can address their respective limitations and provide a more complete view of cloud/aerosol properties and their impacts (Qin et al., 2016; Fang et al., 2024).

Overall, recent studies have shown the importance of the cloud-aerosol transition zone aggregates into the radiative balance, estimating its effects in the longwave and shortwave spectral bands, and showing its non-negligible frequency and extension. However, despite advances in combining ground-based and satellite lidar observations for tropospheric cloud and aerosol research, consistent representation of TZ conditions (i.e., TZ characterization, frequency and extension) by both approaches remains unexplored. This study aims to evaluate the respective capabilities of each instrument by presenting TZ distributions derived from coincident ground-based and spaceborne lidar observations across different atmospheric conditions. Specifically, we evaluate situations where the two methods agree or disagree, highlighting the advantages and limitations of each, as well as their level of agreement. This combination contributes to a better understanding of current knowledge on TZ conditions, including their frequency of occurrence, horizontal extent, and vertical distribution.

https://doi.org/10.5194/egusphere-2026-3737
Preprint. Discussion started: 28 August 2026

2 Instruments, Data & Methodology

The schematic diagram in Fig. 1 illustrates the observational approach used in this study. To investigate the suspended aggregates in the atmosphere (clouds, TZ, and aerosols) we analyzed the 2017 datasets of CALIOP lidar observations over the region bounded by 30º–80º N and 10º W–35º E, covering Europe, alongside measurements from several ground-based ALCs (Fig. 2; Table 1).

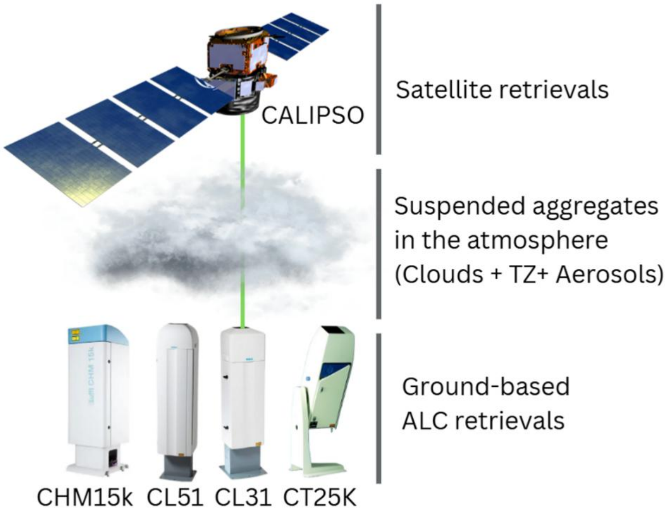

Figure 1: Schematic diagram of the remote sensing observations. Image credits are attributed to NASA for the CALIPSO satellite, OTT HydroMet for the CHM15k, and Vaisala for the CL51, CL31 and CT25K.

2.1 European sites

The method to assess TZ conditions used in the study by Ruiz de Morales et al. (2024) has been taken as a reference for the ground-based observations (more information about the methodology is provided in Section 2.3). The same method has been applied to the GIR CL31 2017 dataset, as well as to the two ALC from the E-profile network (GRW CHM15k and BUR CL51). These locations are very close to CALIPSO ground-tracks (with most CALIPSO profiles being within 5 km). The analysis of these two locations is shown in Section 3.1 with several case studies. Finally, we applied a simplified version of the methodology to the Cloudnet 2017 ALC datasets to have a more complete overview of the ground-based observations across the diverse climatic conditions of the European region. Both the E-profile and Cloudnet networks are part of the Aerosol, Clouds and Trace Gases Research Infrastructure (ACTRIS). Note that for GIR C31, GRW CHM15k and BUR CL51, the original ALC dataset was used and processed with the Cloudnetpy algorithm (Tukiainen et al., 2020). Contrarily, the ALC datasets from the CLOUDNET network had already been processed with Cloudnetpy. Not having the original ALC data forced us to use a simplified version of the method to detect TZ conditions (see Section 2.3).

In this context, BUR, GIR, GRA provide information on the western Mediterranean, and LIM on the eastern Mediterranean, with hot, dry summers and mild, wet winters; CHB, JUL, PAL and GRW represent northwestern European maritime climate with mild winters and humid summers; LIN, MUN and SFH of continental climate, with cold winters and hot, dry summers (SFH is located at 2653 m in the Alps mountain range, and MUN is also influenced by the alpine climate, which makes them particularly interesting); NOR and KEN present a subarctic climate, with cold winters and mild, humid summers; and NYA, located in Svalbard, presents Arctic climate conditions.

https://doi.org/10.5194/egusphere-2026-3737
Preprint. Discussion started: 28 August 2026

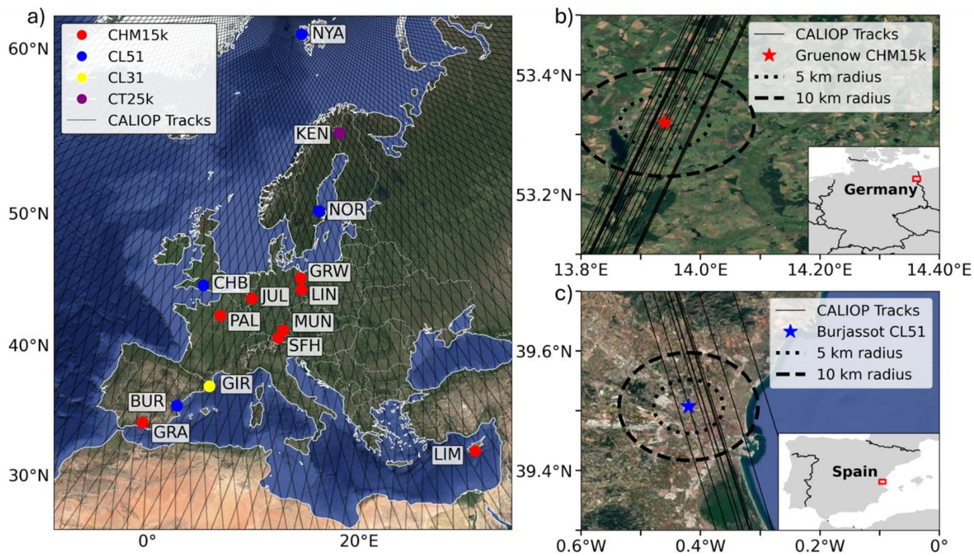

Figure 2: Location of the observational sites. a) Location of the ALC sites contributing to this study along with CALIPSO ground tracks; b) Location of GRW CHM15k, along with CALIPSO's closest profiles; c) Same as (b) but for BUR CL51. Base map © Google Earth 2025.

Table 1 Site location and instrumentation, sorted by latitude.

Station code	Location	Country	Latitude	Longitude	Altitude	ALC type	Network	Daily Files
NYA	Ny-Ålesund	Norway	78.923°N	11.922°E	19 m	CL51	CLOUDNET	365
KEN	Kenttärova	Finland	67.987°N	24.243°E	354 m	CT25K	CLOUDNET	298
NOR	Norunda	Sweden	60.086°N	17.479°E	46 m	CL51	CLOUDNET	164
GRW	Gruenow	Germany	53.315°N	13.934°E	56 m	CHM15k	E-PROFILE	365
LIN	Lindenberg	Germany	52.208°N	14.118°E	104 m	CHM15k	CLOUDNET	364
CHB	Chilbolton	United Kingdom	51.144°N	1.439°W	85 m	CL51	CLOUDNET	364
JUL	Jülich	Germany	50.908°N	6.413°E	111 m	CHM15k	CLOUDNET	362
PAL	Palaiseau	France	48.717°N	2.209°E	156 m	CHM15k	CLOUDNET	365
MUN	Munich	Germany	48.148°N	11.573°E	538 m	CHM15k	CLOUDNET	358
SFH	Schneefernerhaus	Germany	47.417°N	10.977°E	2653 m	CHM15k	CLOUDNET	365
GIR	Girona	Spain	41.962°N	2.829°E	115 m	CL31	–	306
BUR	Burjassot	Spain	39.507°N	0.420°W	89 m	CL51	E-PROFILE	283
GRA	Granada	Spain	37.164°N	3.605°W	680 m	CHM15k	CLOUDNET	361
LIM	Limassol	Cyprus	34.677°N	33.038°E	10 m	CHM15k	CLOUDNET	360

Note: Altitude values are meters above mean sea level (a.m.s.l.)

2.2 Instruments

2.2.1 Spaceborne Lidar: CALIOP

The CALIPSO mission is a joint project between NASA (the National Aeronautics and Space Administration) and the French Space Agency (CNES; Centre National d'Études Spatiales). Launched on 28 April 2006, CALIPSO operated as part of the A-Train satellite constellation, which included satellites such as Aqua, CloudSat, PARASOL, and Aura, maintaining a sun-synchronous orbit at an altitude of 705 km with a 99-minute orbital period. With an orbit inclination of 98º, the satellite provided global coverage from 82º N to 82º S, with ground tracks repeating every 16 days (Winker et al., 2010). On 13 September

2018, CALIPSO underwent a planned orbital manoeuvre, lowering its altitude to 688 km to rejoin CloudSat with the established C-Train constellation, until 1 August 2023 when the CALIPSO mission ended.

CALIPSO is equipped with three co-aligned, near nadir instruments: CALIOP, the Imaging Infrared Radiometer (IIR), and a Wide Field Camera (WFC). CALIOP operates at 532 nm and 1064 nm wavelengths, with polarization sensitivity at 532 nm, providing high-resolution vertical profiles of clouds and aerosols. The laser operates at a pulse rate frequency of 20.16 Hz, with a pulse length of approximately 20 ns (Winker et al., 2010). Each laser generates 220 mJ of pulse energy at both wavelengths. Beam expanders are employed to reduce the angular divergence of the transmitted laser beam, producing a beam diameter of 70 m at the Earth's surface, which corresponds to a nominal laser beam divergence of 100 µrad (Hunt et al., 2009; Mamouri et al., 2009).

For this research, we used all orbit (day and nighttime) data products of the "CALIPSO v.4.51 Lidar Level 1B profile data" and the "Level 2 v4.51 products of clouds, aerosols and merged layers". The level 1 data includes calibrated and geo-located single-shot lidar profiles at the highest resolution, while the level 2 products include the layer detected products. The vertical resolution of the CALIOP data is 30 m from the surface to 8.2 km and 60 m from 8.2 to 20.2 km (Thorsen et al., 2011). The level 1 products have a horizontal resolution of 300 m from the surface to 8.2 km and 1 km from 8.2 to 20.2 km. The level 1 dataset was used to obtain the *Total Attenuated Backscatter* at 532 nm (β'_{532}) and at 1064 nm (β'_{1064}), and the satellite overpass at the studied locations (BUR and GRW), obtaining the closest profiles at those locations. The level 2 dataset provides spatial and optical information for up to 15 layers of suspended particles for each profile, with a horizontal resolution of 5 km while maintaining the original vertical resolution. This dataset was used to obtain the *layer-averaged attenuated backscatter* at 532 nm $\langle\beta'_{532}\rangle$ and at 1064 nm $\langle\beta'_{1064}\rangle$; the *layer-integrated attenuated total colour ratio* (χ'), as the ratio of $\langle\beta'_{1064}\rangle$ to $\langle\beta'_{532}\rangle$; the *layer-integrated volume depolarization ratio* (δ_V) as the ratio between the perpendicular and parallel 532 nm backscatter components; the mid-layer altitude (z_{mid}); and the Cloud Aerosol Discrimination (CAD) score values for each detected layer with CALIOP.

The CAD algorithm uses probability density functions (PDFs) of five dimensions: $\langle\beta'_{532}\rangle$, χ', δ_V, z_{mid}, and the latitude of the layers detected (Liu et al., 2005, 2009, 2010, 2019). The CAD score ranges from –100 to 100, with positive scores indicating a certain likelihood that the feature is classified as a cloud, whereas negative scores indicate the presence of an aerosol layer. The confidence in the layer classification is indicated by the magnitude of the CAD score: $|CAD| \geq 70$ is considered as high-confidence range (HC), $70 > |CAD| \geq 50$ as middle-confidence (MC), $50 > |CAD| > 20$ as low-confidence (LC) and $|CAD| \leq 20$ as no-confidence range (NCR) (Liu et al. 2010, 2019; Yang et al. 2012). These CAD classifications are used for other *Scene Classification* algorithms, such as the Vertical Feature Mask, aerosol/cloud subtyping algorithms. In our study, after applying some filters, NCR values of the CAD-score and cirrus fringes (layers with CAD = 106) are used to identify the TZ layers (see Section 2.3).

2.2.2 Ground-based Automatic Low-Power Lidar and Ceilometers (ALC)

The ground-based instruments used in this study are ALC with an optoelectronic laser sensor, which can detect up to three cloud layers simultaneously. By employing real-time algorithms, these instruments generate height resolved backscatter profiles, through the analysis of the duration and intensity of the laser pulse backscattered to the ALC (Martucci et al., 2010). The operating range of the CHM15k and CL51 is 15.4 km of altitude, enabling the detection of cirrus clouds. However, layers located at high altitudes such as cirrus clouds or cirrus fringes may be significantly hidden in the noise component of the signal at these high ranges (Martucci et al., 2010).

a. VAISALA CL31, CL51 and CT25K

The Vaisala CL31, CL51 and CT25K use an Indium Gallium Arsenide (InGaAs) diode laser, with backscattered signals detected by a silicon avalanche photodiode (APD) analogue detector (Wagner et al., 2024; Chen et al., 2025). They provide measurements on a vertical range 0–7.7 km for the CL31, 0–15.4 km for the CL51, 0–7.5 km for the CT25K, with 5 m, 10 m, 15.24 m (50 ft) vertical resolution, and 2 s, 6

https://doi.org/10.5194/egusphere-2026-3737
Preprint. Discussion started: 28 August 2026

s, 15 s temporal resolution, respectively. The CL31 and CL51 lasers emit 110 ns-long pulses at 910 nm wavelength with pulse repetition rates of 10.0 kHz (CL31) and 6.5k Hz (CL51), respectively. The CT25 emits 100 ns-long pulses at 905 nm wavelength with a repetition rate of 5.57 kHz. According to the manufacturer, the pulses have a nominal energy of 1.2, 3.0, 1.6 µJ and the average laser power are 12, 19.5 and 8.9 mW, respectively (see Table 2 for technical information).

b. LUFFT CHM15k

The Lufft CHM15k uses photon counting technology, operating at 1064 nm wavelength. It has a maximum range of 15.4 km with a minimum vertical resolution of 5 m in the near range (up to 150 m) and 15 m resolution above, and a temporal resolution of 2 s. The laser pulse duration is 1 ns with a pulse energy of 8 µJ, and a repetition rate of 5–7 kHz (see Table 2 for technical information).

Table 2 ALC technical data

ALC parameters	CHM15k	CL31	CL51	CT25K
Manufacturer	OTT HydroMet (former Lufft)	Vaisala	Vaisala	Vaisala
Wavelength (nm)	1064	910	910	905
Maximum range (km)	15	7.7	15.4	7.5
Minimum resolutions (m, s)	5, 2	5, 2	10, 6	15.24, 15
Average laser power (mW)	50	12	19.5	8.9
Pulse duration (ns)	~1	110	110	100
Pulse repetition rate (kHz)	5–7	8.192	6.5	5.57
Energy per pulse (µJ)	8	1.2	3	1.6

2.3 Transition Zone Observations

To assess TZ conditions from a ground-based perspective, we followed the method proposed by Ruiz de Morales et al. (2024), which involves applying different sets of thresholds on the signal-to-noise ratio (SNR), and the SNR-screened backscatter (β) variables used for cloud detection in the Cloudnetpy algorithm. More specifically, TZ conditions are defined as situations in which cloud detection changes when switching between a strict and a relaxed set of thresholds, which are used to delineate the boundary between cloudy and cloudless conditions. For the strict situation, the algorithm uses the default threshold values; a signal-to-noise ratio threshold (SNRth) of 5 and a backscatter threshold (Bth) of 20×10^{-6} $m^{-1}sr^{-1}$. These set of threshold values are consistent with those implemented by the manufacturer algorithm Vaisala (Ruiz de Morales et al., 2024). For the relaxed situation, the thresholds are reduced to SNRth = 4 and Bth = 3×10^{-6} $m^{-1}sr^{-1}$. This approach was applied to three ALCs for which the original raw ceilometer data are available: GIR CL31, BUR CL51 and GRW CHM15k (Fig 3a; case studies are presented in Section 3.1). A simplified version of the method was applied to the CLOUDNET ALC data. Since CLOUDNET data has already been processed and the SNRth cannot be modified, TZ conditions for the ground-based ALC data (e.g., in Section 3.2) are defined solely by changes in detections when switching from Bth = 20×10^{-6} $m^{-1}sr^{-1}$ to Bth = 3×10^{-6} $m^{-1}sr^{-1}$, while keeping SNRth fixed at 5.

In this study, a "hit" corresponds to a profile containing more than one backscatter value classified as cloudy, and the cloud occurrence (CO) is then quantified as the percentage of hit profiles, identified using the default set of thresholds, relative to the total number of processed profiles. Figure 3 shows the percentage of hits as a function of the threshold combinations. In Fig 3a, the method is applied to the GRW, BUR and GIR ALCs, showing the Bth values for both SNRth = 4 and SNRth = 5. The hit profile shape of GIR ALC resembles that reported by Ruiz de Morales et al. (2024), despite being based on a different year (2017 instead of 2022), confirming the robustness of the method for the same instrument and location. This profile shape is characterized by near 100% hit values for Bth < 0.2×10^{-6} $m^{-1}sr^{-1}$, and near 0% values for Bth > 500×10^{-6} $m^{-1}sr^{-1}$. A plateau area is observed for 5×10^{-6} $m^{-1}sr^{-1}$ < Bth < 70×10^{-6} $m^{-1}sr^{-1}$, while sharper transitions for 0.3×10^{-6} $m^{-1}sr^{-1}$ < Bth < 5×10^{-6} $m^{-1}sr^{-1}$ and 70×10^{-6} $m^{-1}sr^{-1}$ < Bth < 500×10^{-6} $m^{-1}sr^{-1}$. The BUR and GRW ALCs show a similar hit profile shape pattern, however, their plateau regions are

https://doi.org/10.5194/egusphere-2026-3737
Preprint. Discussion started: 28 August 2026

less extended, and less gradual, making the decline from cloud-free to cloud more pronounced. Using the default threshold configuration (Bth = 20×10^{-6} m^{-1}sr^{-1} and SNRth = 5), the CO for the 2017 dataset is 26.1% for GIR CL31, 26.1% for BUR CL51, and 65.7% for GRW CHM15k. While for the relaxed set of thresholds (Bth = 3×10^{-6} m^{-1}sr^{-1} and SNRth = 4) the CO is 33.5%, 40.1%, and 76.6%, respectively. By comparing the number of hits obtained under relaxed and strict threshold configurations, TZ conditions account for 7.3% of the total number of profiles in GIR, 14.0% in BUR, 10.9 in GRW. As expected, the less restrictive SNRth = 4 results in a higher number of hits compared to the default SNRth = 5 value, which is particularly apparent for Bth between 0.2 and 20 (× 10^{-6} m^{-1} sr^{-1}). Nevertheless, the overall impact of changing the SNRth from 5 to 4 is relatively small. For example, the number of CO hits (Bth = 20 × 10^{-6} m^{-1}sr^{-1}) increases from 33.4 to 33.5% for GIR CL31, from 36.7 to 40.1% for BUR CL51, and from 75.4 to 76.6% for GRW CHM15k when moving SNRth = 5 to SNRth = 4. In addition, differences in the local climatology contribute to the observed variability in CO, as GIR and BUR are Mediterranean sites while GRW is characterized by a northwestern maritime European climate, which is associated with a higher frequency of cloudy conditions.

The dependence of cloud detection on Bth for SNRth = 5, for all the ALCs used in this study, including all CLOUDNET network ceilometers, as well as the GIR, BUR and GRW ALCs, is shown in Fig. 3b. Most ALCs show a similar pattern shape; however, this behaviour is not consistent across all ALC, and it depends on the climatological characteristics of the observational site. In particular, the four Mediterranean sites (GIR, BUR, GRA and LIM) clearly have lower CO compared to the other sites, with CO values of 26.1%, 26.1%, 25.0% and 15.0% respectively. Nevertheless, the profile shape of GRA and LIM is quite different to the other two Mediterranean sites. The plateau area in GRA is barely discernible and is absent in LIM. Similarly, in PAL, the shift between cloud-free and cloud is constantly gradual, but with a higher CO of 62.1%. A possible explanation for this behaviour is the high presence of fog and/or polluted air masses, as PAL is located within the Paris metropolitan area. Other sites, such as LIN, JUL, and MUN, also show a relatively narrow plateau area that is slightly shifted toward lower Bth values. At NYA, the plateau area spans between 1 × 10^{-6} m^{-1} sr^{-1} and 7 × 10^{-6} m^{-1} sr^{-1}, although it is not strongly pronounced. CHB and SFH show a CO of 66.0%, and 56.1%, respectively, with clearly identifiable plateau region extending from 3 × 10^{-6} m^{-1} sr^{-1} to 20 × 10^{-6} m^{-1} sr^{-1}. Finally, NOR and KEN hit profile shapes are similar to that of GIR, but with a higher overall CO, 68.7% and 72.4%. In both cases, the plateau region is shifted to lower Bth values: between 1 × 10^{-6} m^{-1} sr^{-1} and 10 × 10^{-6} m^{-1} sr^{-1} for NOR, and between 0. 4 × 10^{-6} m^{-1} sr^{-1} and 10 × 10^{-6} m^{-1} sr^{-1} for KEN. In conclusion, the transition between aerosol and cloud conditions as observed by ceilometers is gradual. Consequently, cloud detection is sensitive to the choice of threshold values. However, the characteristics of the observed gradual transition may depend on other factors such as the instrument used, the climatological region, aerosol loading, and atmospheric water-vapour content (Wiegner et al., 2014; Kotthaus et al., 2016). For example, Vaisala ceilometers operate at 910 nm, within a water-vapour absorption band (~ 940 nm), which may influence the measured backscatter signal under varying humidity conditions (Chen et al., 2025).

https://doi.org/10.5194/egusphere-2026-3737
Preprint. Discussion started: 28 August 2026

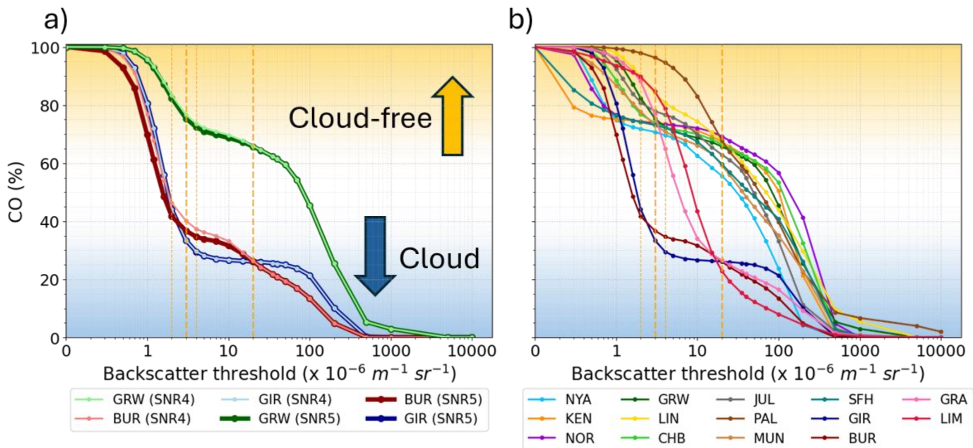

Figure 3: Sensitivity of ALC cloud detection to Bth and SNRth. a) Cloud Occurrence (CO) for different Bth values at SNRth = 4 and SNRth = 5, for the GRW (green), BUR (red) and GIR (blue) ALCs; b) Same as (3a), applied to all ALCs, but only with SNRth = 5. Thick orange dashed lines correspond to the set of Bth threshold used for characterizing the TZ (Bth = 20 × 10^{-6} m^{-1} sr^{-1} and Bth = 3 × 10^{-6} m^{-1} sr^{-1}). Thin orange dashed lines correspond to the uncertainty Bth threshold values for TZ detection (Bth = 4 × 10^{-6} m^{-1} sr^{-1} and Bth = 2 × 10^{-6} m^{-1} sr^{-1}).

To assess the TZ from the satellite perspective, we followed the approach of Ruiz de Morales et al. (2026). Specifically, considering the TZ as the layers within the no-confidence range (NCR; -20 ≤ CAD ≤ 20) of CALIOP's CAD-Score, and the layers classified as cirrus fringes (CAD = 106). To avoid an overestimation of TZ conditions (i.e., to avoid the impact of artifacts), we applied the same filters used in that study: (a) a filter to exclude unrealistic values, just letting through layers with $0 \leq \langle \beta'_{532} \rangle \leq 1$, $0 \leq \chi' \leq 2$, and $0 \leq \delta_V \leq 2$; (b) a filter to exclude layers with z_{mid} detected above the tropopause; (c) a filter to reduce the impact of multiple scattering attenuation from thick layers, excluding features with IAB QA factor < 0.7; where the IAB QA is the variable "integrated attenuated backscatter above a feature quality assessment" provided by CALIPSO products.

Applying these filters to the CALIOP Level 2 dataset over Europe results in the exclusion of 72.2% of the potential TZ layers (layers with -20 ≤ CAD ≤ 20 or CAD = 106). The IAB QA filter is the most restrictive filter, accounting for the exclusion of 59.4% of the TZ layers. The strict filtering procedure also affects the other categories, removing 23.0% of layers classified as clouds (20 < CAD ≤ 100), and 40.7% of the layers classified as aerosols (-100 ≤ CAD < -20). Differences are observed between the daytime and nighttime datasets. For nighttime conditions, 17.2% of clouds, 36.6% of aerosols, and 73.9% of TZ are removed. Whereas, for daytime conditions, 27.0% of clouds, 46.7% of aerosols, and 70.1% of TZ are removed.

As this study retains only layers with a well-defined physical meaning, the reported results should be considered as a lower bound on the true frequency of TZ occurrences.

3 Results & Discussions

This section firstly presents a comparison of the two methods applied to several atmospheric conditions selected from CALIOP overpasses to the ground-based ALCs. By focusing on these coinciding observations, we assess the specific potentials and limitations of each method across different atmospheric conditions, as well as the level of agreement between CALIOP and ALCs. Secondly, to evaluate the TZ spatial distribution and consistency of the two methods, we apply the ground-based approach to all the ALCs used in the study, while simultaneously employing the satellite approach to the CALIOP observations over Europe for the same time period.

3.1 Sampled Atmospheric Conditions

To compare the ground-based ALC and CALIOP retrievals, we used observations from the GRW CHM15k and the BUR CL51, which are the ALCs with the shortest distance (i.e., < 4 km) to CALIPSO's ground-track. During the study period, CALIPSO passed over GRW site at ~1:33 UTC during nighttime on a descending orbit and over BUR site at ~13:18 UTC during daytime on an ascending orbit, with a repeat cycle of 16 days. Over the 2017 period, there were 21 coincidences of CALIPSO over GRW and 18 coincidences over BUR. From these coincidences, 8 case studies were selected, with 5 nighttime (GRW) and 3 daytime (BUR) events corresponding to five different atmospheric aerosol and cloud conditions (Table 3): PBL aerosols in cloud-free conditions (case studies 1 and 2), high-altitude semi-transparent cirrus clouds (cases 3 and 4), low-level clouds (case 5), dense tropospheric clouds attenuating both ground-based and satellite lidar signals (cases 6 and 7), and multi-layer cloud structures (case 8).

For each case study, we analyze the raw backscatter profiles of CALIOP and ALC, compare the closest profiles, and evaluate the final (cloud-TZ-aerosol) classification from the satellite and ground-based perspective.

Table 3 Summary of the sampled atmospheric conditions

Case study	Atmospheric Condition	Date & Time overpass (Day or Nighttime dataset)	Location	ALC type	Distance between CALIOP closest profile to ALC
1	Cloud-free & PBL aerosols	07/08/2017 01:32:49 UTC (N)	GRW	CHM15k	1.01 km
2		05/01/2017 13:18:33 UTC (D)	BUR	CL51	3.24 km
3	Cirrus clouds	01/04/2017 01:33:06 UTC (N)	GRW	CHM15k	3.36 km
4		06/02/2017 13:18:58 UTC (D)	BUR	CL51	1.92 km
5	Low-level clouds	29/12/2017 01:33:16 UTC (N)	GRW	CHM15k	1.61 km
6	Dense tropospheric clouds	21/01/2017 13:18:47 UTC (D)	BUR	CL51	0.10 km
7		24/09/2017 01:32:54 UTC (N)	GRW	CHM15k	0.25 km
8	Multi-layer cloud structures	26/10/2017 01:32:44 UTC (N)	GRW	CHM15k	3.67 km

3.1.1 Cloud-free & PBL Aerosols

Figures 4a and 4b show the 532 nm attenuated backscatter coefficient, $\langle\beta'_{532}\rangle$, retrieved by CALIOP and the backscatter signal at 1064 nm (β) acquired by the CHM15k. The vertical white lines indicate the profiles with the closest spatial and temporal coincidences between CALIOP and the ALC; in this case, the closest CALIOP profile over GRW occurred at 53.3186º N 13.9550º E, at a distance of 1.01 km from the GRW CHM15k location (53.315º N 13.934º E) at 01:32:49 UTC. In Fig. 4a, the x-axis represents a horizontal window of ±10 km around the CALIOP profile closest to the ALC location, corresponding to 58 CALIOP single profiles. Whereas in Fig. 4b it represents the ALC backscatter on a temporal window of ±16 minutes around the satellite overpass. Even though both lidar signals appear quite noisy, especially CALIOP, the ground-based ALC has higher vertical and temporal resolution. It should be noted that CALIOP data show a change in resolution around 8.2 km altitude, resulting from distinct vertical and horizontal resolutions of the CALIOP measurements (see Section 2.2.1).

In this case, no clouds were detected in the vicinity of the coincidence. A horizontally stable aerosol structure within the PBL is observed before and after CALIPSO's overpass at GRW's site (Fig. 4a). The ground-based measurements also show the temporally stable PBL aerosol layer extending up to approximately 1.8 km (Fig. 4b).

Figure 4c shows the backscatter profile retrievals of the spatially closest CALIOP profile to the location and the CHM15k temporally closest profile to the CALIPSO overpass. Single profiles of $\langle\beta'_{532}\rangle$ and $\langle\beta'_{1064}\rangle$ from CALIOP, as well as the raw (β_{raw}) and processed (β) backscatter signals from the CHM15k are shown. To reduce the impact of noise and provide a clearer representation of the atmospheric condition, the average

https://doi.org/10.5194/egusphere-2026-3737
Preprint. Discussion started: 28 August 2026

of multiple profiles is also shown. For CALIOP, the average is calculated using all the profiles within ±10 km around the closest profile to the location, while for the CHM15k the average includes all the ALC profiles within the temporal window of ±16 minutes of CALIPSO overpass time. These ranges were selected to provide sufficient and comparable sampling, considering the instrument resolution and a typical horizontal wind speed. They are only used to represent the case studies and do not influence the final feature frequency results. The high values of $\langle \beta'_{532} \rangle$, and $\langle \beta'_{1064} \rangle$, detected near 0 km, correspond to the surface signal return.

The final cloud-TZ-aerosol classification for the 07/08/2017 case, obtained after applying all filters to both methodologies, is represented in Fig. 4d. Both methods consistently identify a PBL aerosol structure extending up to approximately 2 km of altitude. The ALC final classification also reveals some dispersed TZ detections at the top of the PBL aerosol layer. These values may not correspond to the TZ between clouds and aerosols, but rather the aerosol – clear sky boundary with higher backscatter (but also noise), so aerosols at the edge of the PBL may not be detected with confidence.

Figure A1 shows an atmospheric condition similar to that shown in Fig. 4, but for BUR CL51, and daytime observations. Thus, the backscatter retrievals also show a clear sky with an aerosol layer located below 1 km. One difference in retrieval is that BUR CL51 data resolution is every 1 min while GRW is every 15 s. Moreover, daytime lidar data is noisier than that of nighttime. The profile comparison also shows a clear sky, with some low but detectable backscatter signals within the lowest kilometre. The final classification shows PBL aerosols with some TZ detections above the PBL for the BUR CL51, while CALIOP shows a TZ layer within the lowest 400 m. These findings are consistent with previous CALIPSO validation studies, which have shown that for cloud-free conditions, both satellite and ground-based lidars are capable of reliably detecting typical urban PBL aerosol layers (Kim et al., 2008).

https://doi.org/10.5194/egusphere-2026-3737
Preprint. Discussion started: 28 August 2026

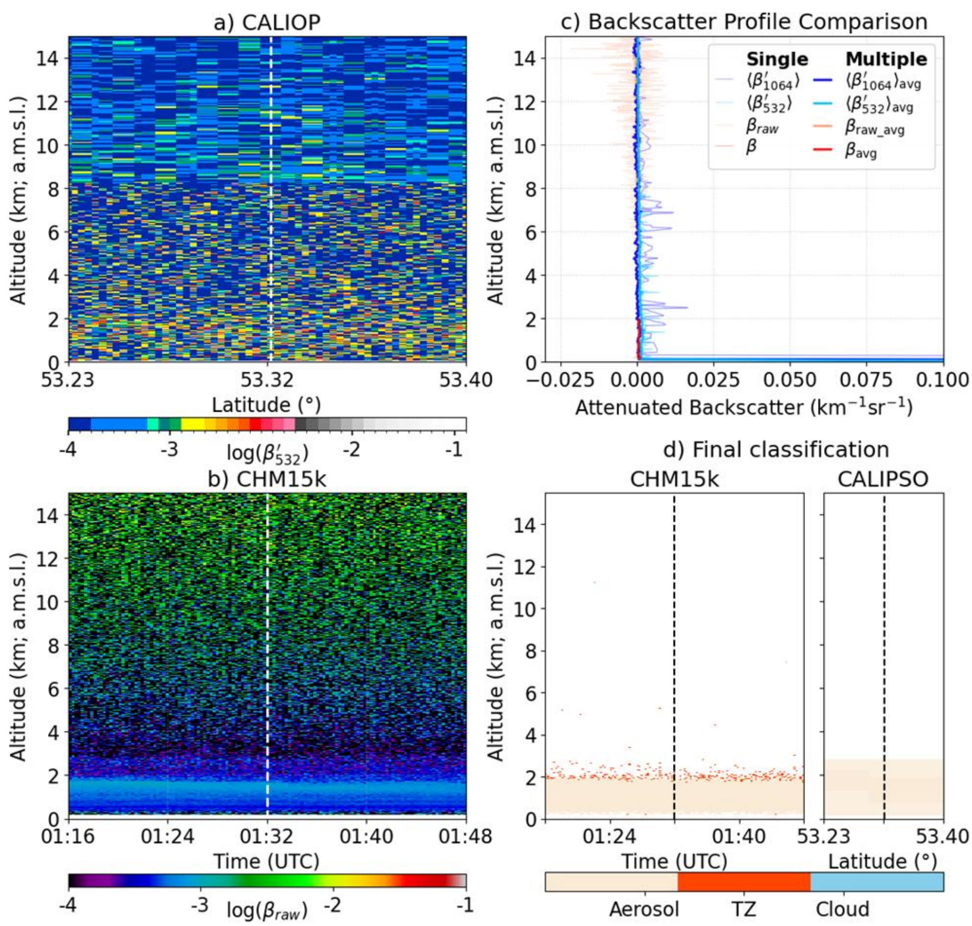

Figure 4: Comparison between concurrent ground-based and satellite lidar retrievals on 07/08/2017, showing a cloud-free atmosphere and PBL aerosols over the GRW CHM15k ALC. a) CALIOP 532 nm attenuated backscatter coefficient from 53.23 to 53.40º N (which corresponds to 10 km along the ground-track, before and after the closest profile to the ALC location). White line corresponds to the closest CALIOP profile to the ground-based ALC location; b) Raw backscatter profiles of the GRW CHM15k between 1:16 UTC and 1:48 UTC (correspond to 16 minutes before and after the satellite overpass time). Note that the signal is represented as the logarithm of the β_{raw} signal. White line corresponds to the profile closest in time to the CALIPSO's overpass; c) Closest vertical profiles of CALIOP ⟨β'_{532}⟩ and ⟨β'_{1064}⟩ and CHM15k β and β_{raw}; d) Final classification as clouds, TZ and aerosol layers. Left panel represents the CHM15k classification, whereas the right panel represents the CALIOP classification.

3.1.2 Cirrus Clouds

Several coincidences between ground-based and satellite lidars with cirrus clouds observations were found in the analysis (e.g., 20-06-2017, 23-08-2017 in Gruenow; not shown). Overall, these cases show that cirrus clouds can be detected by both lidars. However, depending on cloud optical depth (COD), cloud base height (CBH), and cloud top height (CTH) ground-based lidar measurements may fail to fully capture cirrus layers due to signal attenuation with height. Furthermore, as our objective is to assess the TZ layers with physical meaning, our filters are quite strict to ensure that instrumental artifacts are removed and not processed. This limitation leads to an underestimation of cirrus clouds and the associated TZ features at high altitudes (e.g., cirrus fringes) in ground-based observations.

https://doi.org/10.5194/egusphere-2026-3737
Preprint. Discussion started: 28 August 2026

Figure 5 presents a case of cirrus cloud observations over GRW on 01/04/2017, when the shortest distance between the ground-based and the satellite lidars profiles was 3.36 km. Besides, Figure A2 shows a case of cirrus clouds over BUR on 06/02/2017, with a closest separation of 1.92 km.

In Fig. 5a, a cirrus cloud extending from 10 to 12 km is clearly identified from CALIOP backscatter retrievals. From the ground-based perspective (Fig. 5b), the same layer is also detectable but appears optically thinner, likely due to increasing signal attenuation with altitude. This layer can be clearly identified in the backscatter comparison where both methodologies show enhanced backscatter values at this height. However, in the final classification, a large fraction of the GRW CHM15k detections are filtered out, showing that it is a very restrictive method, designed to avoid classifying noisy values. CALIOP classifies this layer as a HC cloud from 9.9 to 12.0 km. Additionally, a very thin layer can also be distinguished at about 7 km altitude from the CHM15k backscatter retrievals. This layer is more difficult to identify in the CALIOP backscatter retrievals and in the profile comparison for both systems; nevertheless, in the final classification CALIOP detects a cloud layer at this altitude, while the CHM15k shows some dispersed cloudy and TZ conditions. Both observing systems consistently detect an aerosol layer from the surface up to about 2 km, although the CHM15k additionally shows some dispersed TZ conditions at the top of this aerosol layer.

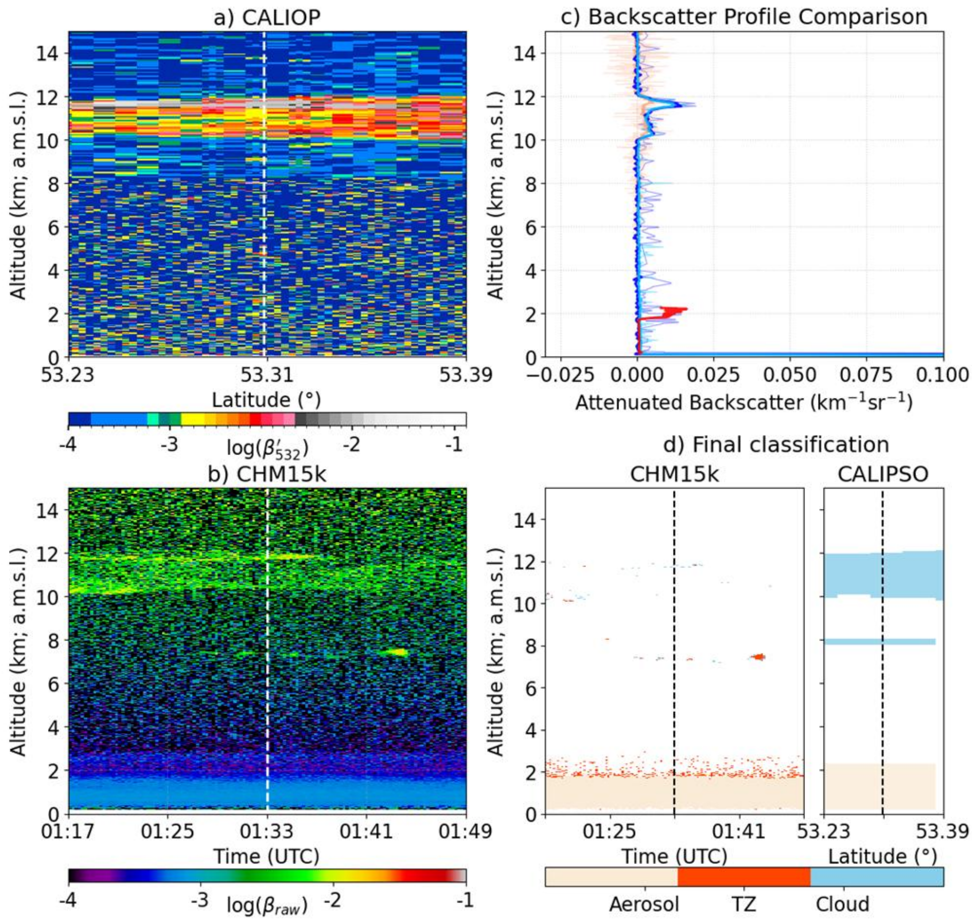

Figure 5: Same as Fig. 4, but for cirrus clouds on 01/04/2017 over GRW. The CALIOP 532 nm attenuated backscatter coefficient spans 53.23 - 53.39º N, while the ALC raw-backscattered is from 01:17 to 01:49 UTC.

https://doi.org/10.5194/egusphere-2026-3737
Preprint. Discussion started: 28 August 2026

Similarly, Fig. A2a shows four layers of cirrus clouds located between 10 and 13 km, along the CALIOP backscatter retrievals. These layers can be clearly identified on the single and multiple averaged profiles. In the final classification, these features are classified as a continuous layer of cirrus clouds between 9.8 and 12.9 km, potentially simplifying the vertically layered structure. From the ground-based perspective, only a thin cirrus layer can be identified at 10.1 km, which can also be identified in the β_{raw_avg} backscatter profile. However, due to the noise at high altitudes, particularly around the mid-day, most of the corresponding detections are filtered out in the final classification. Both lidars also identify a cloud located at 2.6 km, even though this layer is filtered out in the CALIOP final classification as a result of the IAB QA filter, which only retains the layers with sufficient signal quality. The BUR CL51 further detects aerosol layers within the PBL up to 1 km, along with some TZ values at the top of the PBL and in the vicinity of the cloud located at 2.6 km.

3.1.3 Low-level Clouds

A comparison of retrievals for low-level clouds is presented in Fig. 6. In this example, a dense stratocumulus cloud layer is detected by both lidar backscatter retrievals (Fig. 6a and 6b), with CBH at about 1 km. The backscatter profile comparison shows good agreement between both observing systems in terms of the CBH. Besides, the cloud layer is optically thick, leading to strong signal attenuation in both instruments. Consequently, the GRWCHM15k is unable to detect the CTH, while CALIOP has limited sensitivity to the aerosol layer beneath this cloud layer. The final classification for both methods provides a more comprehensive representation of the atmospheric condition. Both methods identify a stratiform cloud layer. However, the ground-based approach, beneath the stratiform cloud, further reveals regions of aerosols, some with enhanced hydration, resulting in the detection of TZ aggregates. CALIOP, in contrast, shows a simplified classification, just identifying the cloud layer between 0.7 to 1.5 km without resolving the underlying TZ structure.

This behaviour, characterized by the detection of TZ layers located right below or in the vicinity of low clouds in ALC observations, has been consistently observed in multiple cases (see for example Ruiz de Morales et al., 2024, Yang et al., 2024, and Hu et al., 2025).

https://doi.org/10.5194/egusphere-2026-3737
Preprint. Discussion started: 28 August 2026

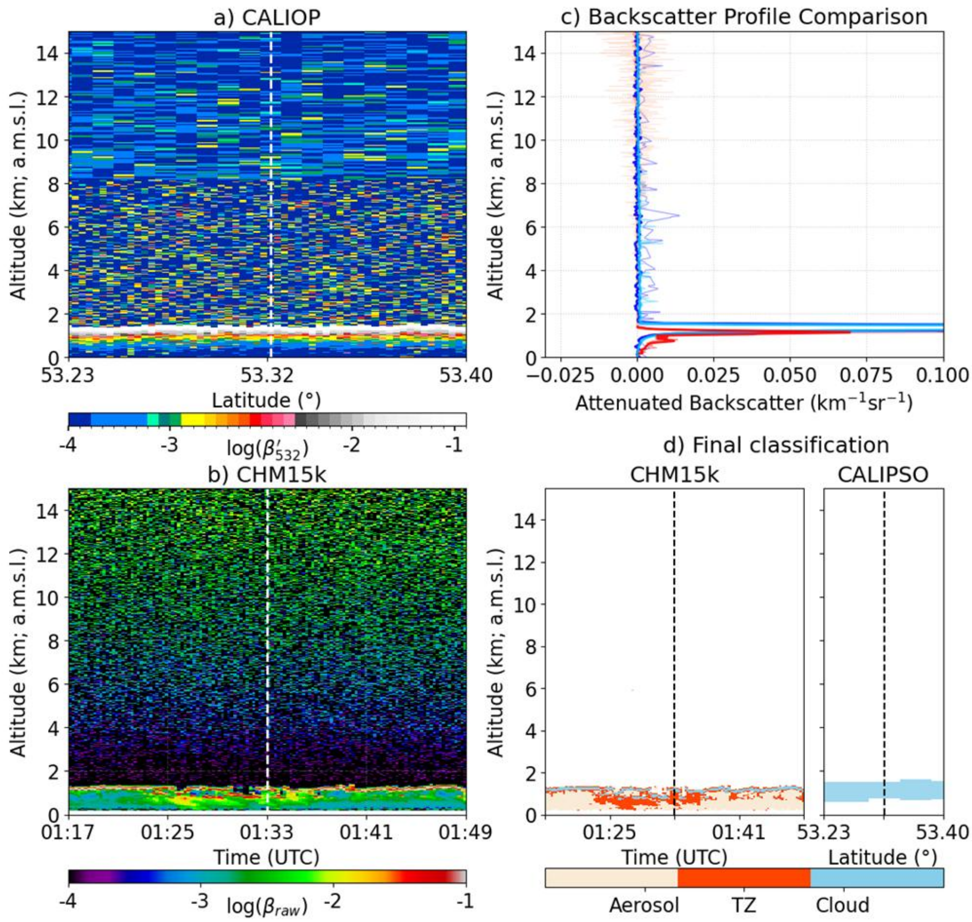

Figure 6: Same as Fig. 4, but for low-level clouds on 29/12/2017 over GRW. The CALIOP 532 nm attenuated backscatter coefficient spans 53.23 - 53.40º N, while the ALC raw-backscattered is from 01:17 to 01:49 UTC.

3.1.4 Dense Tropospheric Clouds

Dense tropospheric clouds represent a main limitation for both methods as they can fully attenuate lidar signals and prevent the laser beam from penetrating optically thick cloud layers. Such clouds can block the laser beam, and/or the return signal from the scattering particles, preventing the detection of other layers. Furthermore, spatially and vertically inhomogeneous cloud distributions at horizontal scales of a few kilometres can further contribute to discrepancies in the determination of CBH and CTH (Kim et al., 2008). Examples of dense atmospheric clouds are illustrated in Fig. 7 and A3.

In Fig. 7, CALIOP backscatter retrieval over BUR shows a cloud layer located between 7.9 and 10.4 km altitude. This cloud layer strongly attenuates the lidar signal preventing a reliable characterization of the atmospheric structures beneath it. Conversely, BUR CL51 detects a cloud layer with CBH at 1.1 km, as well as an aerosol layer below the cloud, with localized regions of enhanced backscatter that are likely associated with hydrated aerosols. Nevertheless, the CL51 lidar signal becomes fully attenuated within the cloud, preventing the detection of atmospheric layers above it.

https://doi.org/10.5194/egusphere-2026-3737
Preprint. Discussion started: 28 August 2026

The CALIOP profile closest to the ALC station shows enhanced backscatter values at around 9.3 km altitude. In contrast, the final CL51 classification provides a detailed characterization of the cloud layer at 1.1 km, the aerosol layer below, and the associated TZ features beneath the cloud, although it cannot observe the atmospheric structure above the cloud.

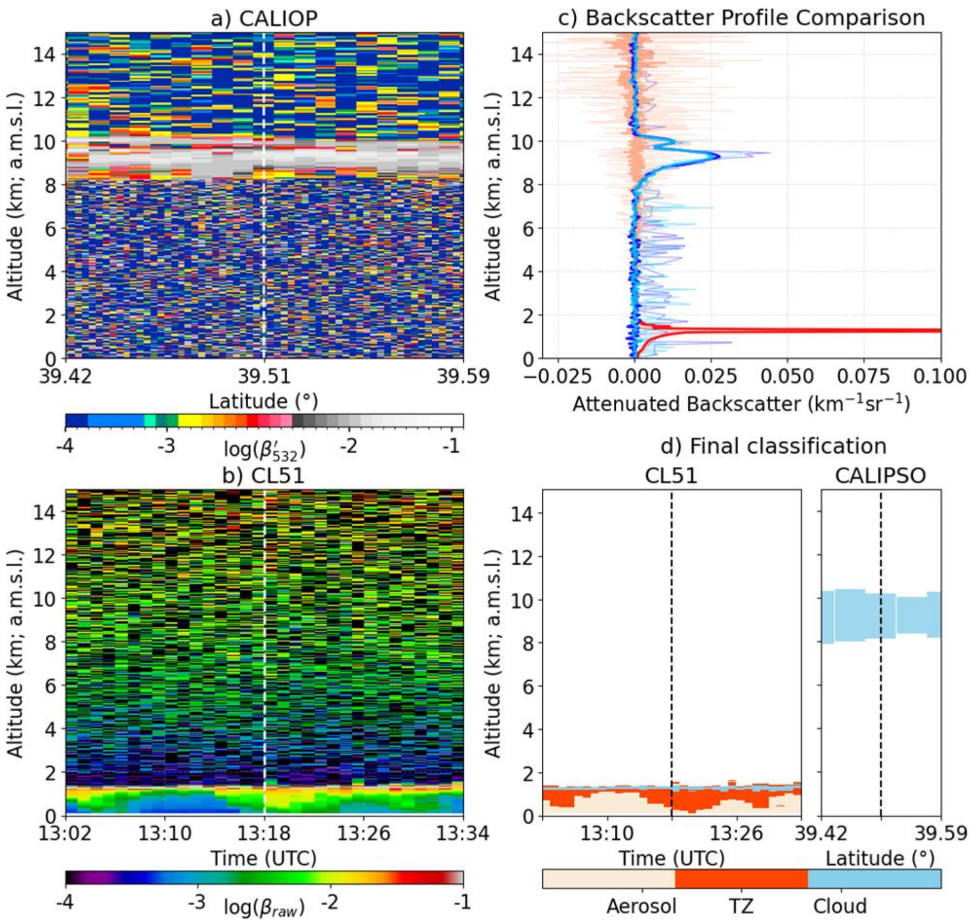

Figure 7: Same as Fig. 4, but for dense tropospheric clouds on 21/01/2017 over BUR. The CALIOP 532 nm attenuated backscatter coefficient spans 39.42 - 39.59º N, while the ALC raw-backscattered is from 13:02 to 13:34 UTC.

Figure A3 shows a similar condition at GRW, with cirrus clouds and a thick low cloud that attenuates both lidars. The GRW CHM15k perceives a strong backscatter signal in the lowest range gates, which fully attenuates the lidar signal above the first 300 m. In contrast, CALIOP detects the cirrus layer between 7.5 and 10.8 km, as well as the top of a cloud layer located at 1.9 km, below which the lidar signal becomes strongly attenuated. In the final classification, the CHM15k identifies only the lowest range gates as cloudy, while CALIOP classifies the cirrus layer with TZ conditions below the cirrus base. Although the cloud at 1.9 km is initially detected and classified by the CALIOP algorithms, it is subsequently filtered out due to the restrictive IAB QA filter.

https://doi.org/10.5194/egusphere-2026-3737
Preprint. Discussion started: 28 August 2026

3.1.5 Multi-layer Cloud Structures

A multilayer cloud structure was observed on 26/10/2017 at GRW by both the ground-based CHM15k and the spaceborne CALIOP lidars (Fig. 8). The backscatter observations from both lidars consistently identify two cirrus cloud layers at 7–8 km and 10–12 km, as well as some clouds embedded with PBL aerosols. The profile comparison highlights the overall good agreement between the two observations.

In the final classification, a cirrus layer with CBH of 10.2 km and CTH of 11.8 km is derived from CALIOP, while the CHM15k shows some scattered cloudy and TZ values between 10.7 and 11.2 km. Both observational methods coincide in a TZ layer observed between 7.6 to 8.1 km, with the CHM15k identifying some cloud values at these altitudes. The CHM15k further resolves lower-altitude layers, detecting a permanent TZ layer between 0.2 to 0.5 km, with cloudy values above this layer around 01:19 UTC and between 01:32 UTC and 01:42 UTC. PBL aerosols are observed from the surface up to 1.3 km, with some TZ values located at the top of the aerosol layer. The original CALIOP CAD-values (before filtering, not shown) show some additional layers that were removed by the IAB QA filter, including two cloud layers from 7.0 to 8.3 km, and 0.2 to 0.7 km, a TZ layer from 9.9 to 10.5 km and 0.2 to 1.1 km, and an aerosol layer from 0.7 to 1.1 km.

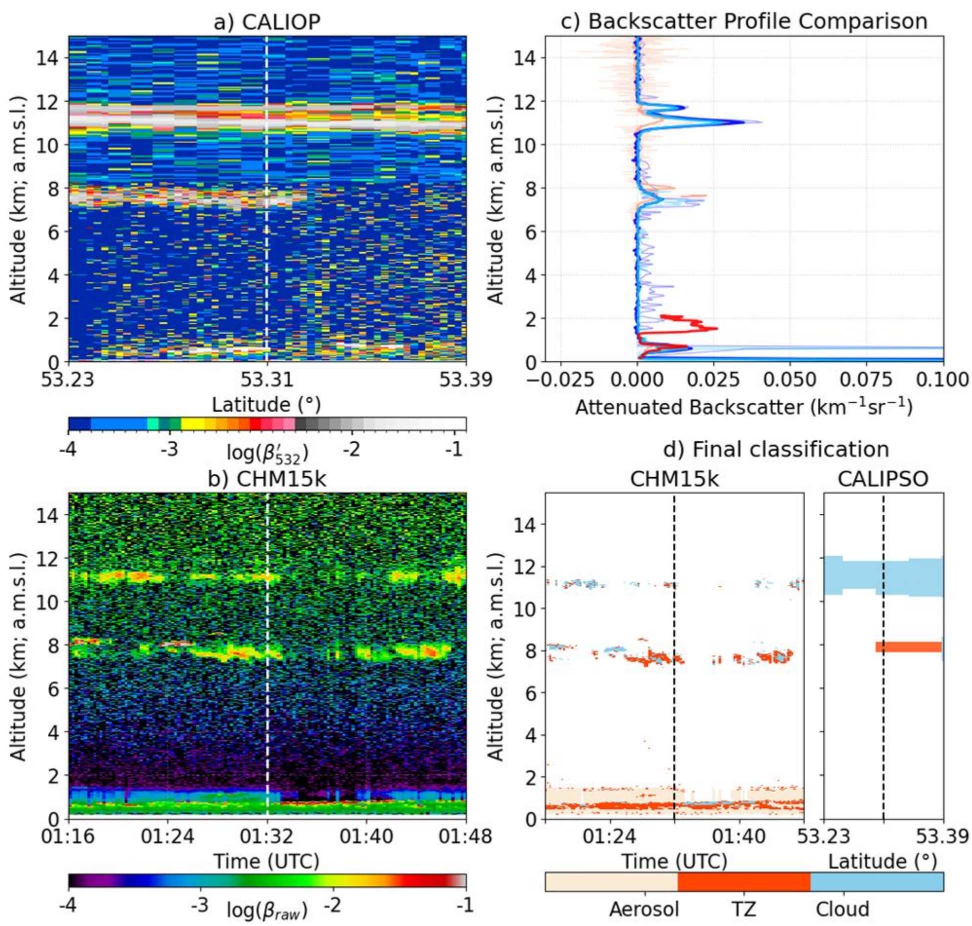

Figure 8: Same as Fig.4, but for multi-layer cloud structures on 26/10/2017 over GRW. The CALIOP 532 nm

https://doi.org/10.5194/egusphere-2026-3737
Preprint. Discussion started: 28 August 2026

attenuated backscatter coefficient spans 53.23 - 53.40º N, while the ALC raw-backscattered is from 01:16 to 01:48 UTC.

As a partial conclusion of this section, the case studies show that TZ detections from ALC and CALIOP observations complement each other well, although some layers were detected by only one method. Ground-based ALC measurements are more effective for detecting TZ conditions at low altitudes; however, their sensitivity decreases for optically thin layers at higher altitudes. In contrast, CALIOP provides better detection of high-altitude TZ layers, although its coarser resolution and "strict" filtering can reduce the detection of layers at lower altitudes, Finally, complete signal attenuation caused by optically thick layers remains as the major limitation for both lidars, leading to an underestimation of TZ occurrence above (for ALC) or below (for CALIOP) dense clouds.

These results agree and complement other studies focused on integrating satellite and ground-based lidar observations. For instance, Kim et al. (2008) validated aerosol and cloud layer structures from CALIOP using a ground-based two wavelength polarization lidar (SNU lidar) in Seoul (Korea), and concluded that simultaneous CALIOP and SNU lidar observations complement each other and can be combined to provide full information on the vertical distributions of aerosols and clouds. In addition, top and base heights of cloud and aerosols are generally in agreement in 0.1 km, particularly for nighttime observations. Kim et al. (2014) used the same instruments and location to study geometric and optical properties of cirrus clouds. Interestingly, they found that about 50% of both lidar profiles were classified as "sub visual" or "optically thin clouds" with COD < 0.3. Perrone et al. (2011), through direct profile comparisons with Raman lidars, also showed that CALIOP can reliably detect aerosol layers at least up to ~0.3 km from ground in cloud-free conditions. Additional comparisons have been made with Raman lidars from EARLINET (Pappalardo et al., 2010, 2014), which aim to provide long term ground-based observations to support spaceborne lidar missions in order to homogenize observations obtained with different instruments.

3.2 Spatial Distributions

This section shows the horizontal and vertical distributions of the atmospheric features, as observed by the satellite and ground-based products. The distributions are assessed in two distinct ways using column integrated measurements that consider the entire vertical atmospheric profile as a single column. First, the column integrated feature frequency (CI-FF) shows the frequency of occurrence of clouds, TZs, or aerosols, regardless of whether another type of layer is present in the same profile. Second, the column- integrated hierarchical frequency (CI-HF), classifies each profile: if a cloud is detected in a profile, this is counted as such (regardless of the other detections); if no cloud but TZ is detected in a profile, that profile is counted as TZ; and if only aerosols are detected, the profile is counted as aerosol. Thus, aerosol profiles do not include clouds or TZ, and TZ profiles do not include clouds.

Figure 9 shows the heatmaps of the CI-FF detected by CALIOP, along with the CI-FF for each of the ALC sites. Table B1 presents the exact CI-FF values represented in Figure 9. As expected, due to the general atmospheric circulation, frequencies of cloud occurrence show a latitudinal dependency (Figure 9a), being clearly higher above 45º N. Also, CALIOP shows slightly higher cloud frequencies in some grid cells over the North Atlantic Ocean, such as the Greenland Sea and North East Atlantic, compared to cells over land Europe and Greenland. Ground-based observations show a similar distribution with higher frequencies over central and northern Europe than over Mediterranean sites. It is worth noting that the ALCs from KEN and GIR reach a lower altitude (7.7 km) compared to the other ALCs (15 km). As the tropopause is lower at polar regions, high clouds are also located at lower altitudes, which may not have such large impact for KEN, whereas it may affect GIR ALC, underestimating features located at high altitudes such as cirrus clouds, or some TZs and aerosols. The sites at lower latitudes, GRA and LIM, are also the ones with less cloud occurrence: 25.0% and 15.0%, respectively, from ground-based point of view, and 34.4% (35–40º N, -5–0º E) and 22.3% (30–35º N, 30–35º E) from CALIOP (Table B1). In general, for cloud detection there is good agreement between the two methods, as both instruments are designed to detect clouds, and thus

https://doi.org/10.5194/egusphere-2026-3737
Preprint. Discussion started: 28 August 2026

observe the same phenomena, because the lidar can see through the other features (e.g., TZ and aerosol layers). As we count column integrated frequencies, when there is a thick layer in the profile (e.g., stratus or deep convective clouds) that attenuates both lidar systems, it will be counted by both, even though one observes from above and the other from below. In such cases, the cloud counted by both systems at the same atmospheric column may not correspond to exactly the same cloud. Regarding TZ and aerosol conditions, there are more differences between the retrievals from the two perspectives. From the satellite point of view the European mean CI-FF is 8.2% for total TZ, and 34.6% for aerosols, considering all profiles. Whereas from the ground-based point of view, aerosol is detected in almost all profiles of all locations (96.9%), while total TZ for all ALC stations is 59.9%. A first explanation for such differences is that aerosol suspensions are mostly concentrated at lower altitudes, which facilitates their detection from the ground-based method, as seen in the case studies of Section 3.1. Additionally, the high (spatial and temporal) resolution of the ground-based method allows aerosol detection within the PBL in almost all profiles. The ground-based method also allows for the detection of aerosols with higher backscatter (probably bigger and hydrated aerosols) mostly located at the top of the PBL, which are classified as TZ detection. This high resolution of ALC also allows for the detection of TZ conditions surrounding most cloud layers, whereas CALIPSO would classify the same layers as just cloud. In some cases, TZ layers are also detected far from clouds. TZ conditions from the satellite point of view are more frequently located in regions with higher cloud occurrence, while aerosol layers are more frequent at northern Africa and Mediterranean regions, probably due to the detection of Saharan dust intrusions, but also by the low cloud frequency in these regions, which allows to detect more aerosol layers. Without applying the filters to the CALIOP datasets, the TZ profile frequency would be 24.5% (29.5% for nighttime and 20.6% for daytime), clouds frequency would be 66.6% (64.7% and 68.1% for daytime), and aerosol frequency 54.6% (68.2% and 44.1%). Note that there were more CALIOP profiles in the daytime dataset than in the nighttime.

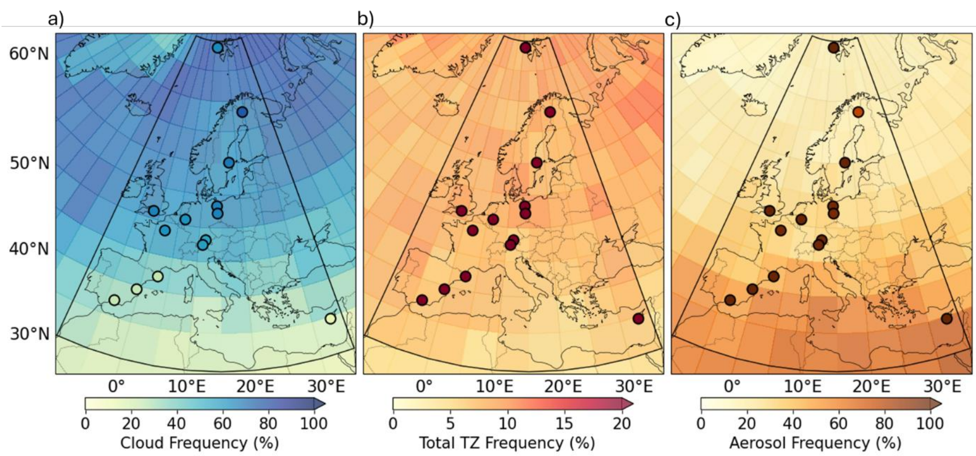

Figure 9: Spatial distribution of the column integrated feature frequency (CI-FF) detected in CALIOP data and in the ground-based ALC observations. a) Cloud frequency by CALIOP (20 < CAD ≤ 100) and for each of the ALC (values with Bth > 20 × 10^{-6} m^{-1} sr^{-1}); b) TZ frequency by CALIOP (-20 ≤ CAD ≤ 20) and by the ALC (values between Bth = 3 × 10^{-6} and Bth = 20 × 10^{-6} m^{-1} sr^{-1}); c) Aerosol frequency by CALIOP (-100 ≤ CAD < -20) and by the ALC (values with Bth < 3 × 10^{-6}). Note that in this plot we used the simplified ground-based method, so SNRth = 5 for all the TZ and aerosol detections. Grid resolution is 5º and each feature has its own scale.

To provide additional context to these results, the TZ layers detected by CALIOP were further assessed using $\langle\beta'_{532}\rangle$, χ', δ_V, and z_{mid} as input variables for the k-means clustering algorithm on the layers with |CAD| ≤ 20, as in Ruiz de Morales et al. (2025). As a result, three TZ subtypes were obtained: the resulting two

https://doi.org/10.5194/egusphere-2026-3737
Preprint. Discussion started: 28 August 2026

clusters, and the cirrus fringes, which correspond to layers with CAD = 106. As described by Ruiz de Morales et al. (2025), Cluster 1 corresponds to layers with optical properties between high-altitude ice clouds and aerosols (e.g., cirrus, aerosols, and wispy cloud fragments), characterized by particle aggregates that are bigger, slightly less reflective, and have higher depolarization ratio than typical aerosols. However, they are smaller, less reflective, and with lower depolarization ratio than non-spherical ice cloud droplets. Cluster 2 correspond to layers with optical properties that lie between water clouds and aerosols at lower altitudes (e.g., large hydrated aerosols). These layers are more variable in size, likely depending on the hydration stage. They are generally bigger, slightly more reflective and non-spherical (with a low depolarization ratio) compared to aerosols, but still, they are smaller and less reflective than liquid water cloud droplets. Figure C1 shows the CI-FF spatial distribution of these subtypes across Europe. Cluster 1 and cirrus fringes are more frequently observed at high altitudes (approximately between 4 to 14 km), especially between latitudes 45º N and 65º N, over central and northern Europe, the North Sea and the North Atlantic Ocean. In contrast, Cluster 2 layers are more frequent at lower heights (from 0 to 8 km, with the highest frequencies from the surface to 2 km) of the Mediterranean basin from 30º N to 45º N and at the Arctic (latitudes over 70º N).

Figure 10 shows the CI-HF detected by CALIOP along with each of the ALC, and Table B2 presents the exact CI-HF values. Figure 11 further complements this information by showing the layer detection height distributions for some sites located in the Mediterranean, Arctic, and Central Europe. When analyzing the CI-HF (profiles can only be classified as cloud, TZ or aerosol/cloud-free, being cloud the most important radiatively, then TZ and finally aerosol), the spatial distribution of TZ layers completely changes, showing more detection frequency at the Mediterranean basin and southern Europe. Still, there are large differences between the two methods. Apart from the methodological reasons already explained, these differences could also be due to the climate (and microclimate) at each location. For instance, the high frequency of TZ detections at PAL (24.9%) may be related to the presence of haze, fog and urban pollution within the Paris metropolitan area (Elias et al., 2009). These conditions characterized by enhanced aerosol loading under high relative humidity lead to an increase in particle hygroscopic growth and lidar backscatter, which then are classified as TZ rather than aerosol (Fig. 11). Whereas the high presence of TZ conditions in GRA and LIM are likely related to frequent Saharan dust intrusions combined with high humidity from the Mediterranean. As shown in previous research, the atmospheric circulation during a Saharan dust intrusion over Europe may pull moist air from the eastern Atlantic and Mediterranean into the dust plume, creating "dust-cloud mixes" with relative humidity up to 70-80 % in the dust layer (Peshev et al., 2022). During these events, some dust particles may become more hydrated, producing aggregates with optical characteristics that fall between clouds and aerosols. These high TZ frequencies can already be observed in the curves of Fig. 3, which show a constant gradual change between cloud and cloud-free (containing aerosol), accounting for a large presence of TZ conditions, particularly in PAL, GRA and LIM. In these locations, TZ detections likely correspond to Cluster 2 aggregates. In BUR, the TZ conditions may be also associated with regional pollution from Valencia, marine aerosols from the Mediterranean Sea, some dust intrusions and high relative humidity (Segura et al., 2017). At GRW and the other ALCs located in central Europe (LIN, JUL, MUN and SFH), TZ layers are likely associated with continental clouds and aerosols processes (Barthlott et al., 2018). In central Europe, the frequent formation and dissipation of fog and low stratus clouds are also influenced by topography and seasonality (Pauli et al., 2022), both of which can affect the occurrence of TZ conditions. In northern Europe and the Arctic (NYA, KEN and NOR), TZ detections are related to polar clouds, which have low optical depth. Observations from campaigns such as "Arctic CLoud Observations Using airborne measurements during polar Day" (ACLOUD) in 2017 near Svalbard reveal complex interactions between the Arctic boundary layer and mid-level clouds (Wendrich et al., 2019).

The CI-HF spatial distribution of aerosol layers shows a much better agreement between the two methods, with higher frequencies in the Mediterranean and lower frequencies at northern latitudes. The stations with the highest aerosol frequency are BUR and GIR, probably explained by the low cloud occurrence (26.1% for both), and not so frequent TZ (10.6 and 7.3%). GRA and LIM also had low cloud frequency (25.0 and 15.0%), but the presence of larger Saharan dust aerosols, which produce strong enough backscatter signals,

https://doi.org/10.5194/egusphere-2026-3737
Preprint. Discussion started: 28 August 2026

may have been classified as TZ instead of aerosol. At central and northern Europe, the ground-based method shows higher detections, compared to the satellite, likely due to the persistent detection of PBL aerosols by the ALC.

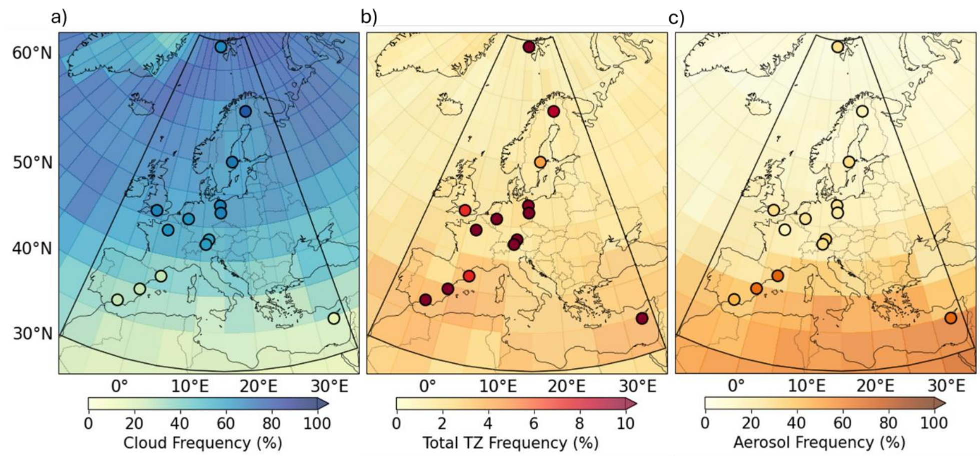

Figure 10: Spatial distribution of the column integrated hierarchical frequency (CI-HF) detected in CALIOP data and in the ground-based ALC observations. a) Cloud frequency by CALIOP (20 < CAD ≤ 100) and for each of the ALC (values higher than Bth = 20 × 10^{-6} m^{-1} sr^{-1}); b) TZ frequency by CALIOP (-20 ≤ CAD ≤ 20) and by the ALC (values between Bth = 3 × 10^{-6} and Bth = 20 × 10^{-6} m^{-1} sr^{-1}); c) Aerosol frequency by CALIOP (-100 ≤ CAD < -20) and by the ALC (values lower than Bth = 3 × 10^{-6}). Note that in this plot we used the simplified ground-based method, so the SNRth = 5 for all the TZ and aerosol detections. Grid resolution is 5° and each feature has its own scale.

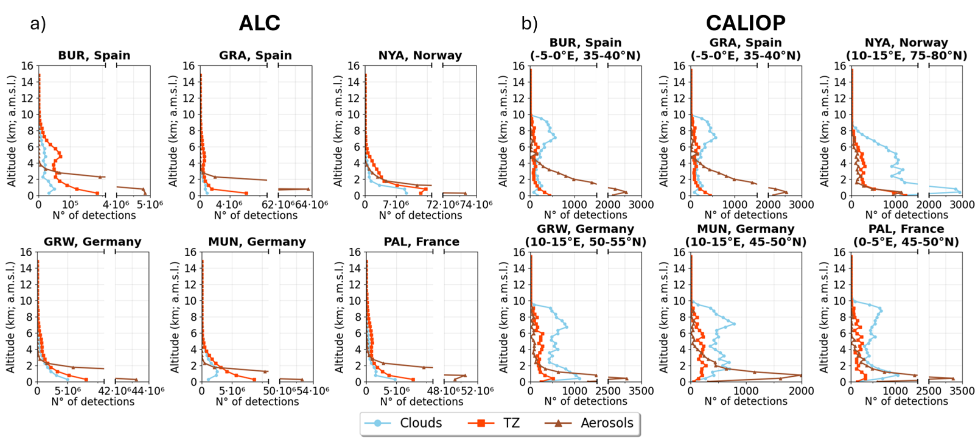

Figure 11: Height distributions of the layer detections in the Mediterranean (BUR and GRA), Arctic (NYA), and Central Europe (GRW, MUN and PAL). a) ALC detections; b) CALIOP detections. Note that y-axis frequency is every 0.5 km, and the x-axis values follow individual scales for each subplot.

https://doi.org/10.5194/egusphere-2026-3737
Preprint. Discussion started: 28 August 2026

4 Conclusions

This study aims to assess the potentials and limitations of two ground-based and space-based active remote sensing techniques for TZ characterization. The goal is to enhance the current understanding of TZ conditions and provide context for their respective interpretation. To this end, TZ distributions over Europe from ground-based ALC and spaceborne CALIOP were assessed. First, case studies of coincidental observations under various atmospheric conditions are presented, which have demonstrated the consistency and limitations of both methodologies. Second, we present the horizontal and vertical spatial distributions of clouds, aerosols, and TZ in two distinct ways: the CI-FF and CI-HF. For cloud detection, there was some variability, although both methods showed good agreement. Clouds were detected in 60.0% of all CALIOP profiles over Europe and in 52.7% of the ALC profiles, with higher frequencies at northern latitudes. However, differences were observed in the detection of aerosols and TZs. When counted as CI-FF, TZ and aerosol detections from ALCs are very high, being detected in 59.9% and 96.9% of all profiles, respectively. Whereas, from CALIOP they are detected in 8.2% and 34.6% of all profiles. These differences can be attributed to the fact that aerosol suspensions are mostly concentrated at low altitudes, which facilitates their detection from the ground-based method, but also due to the high vertical resolution and sensitivity of ALC. When counted as CI-HF, TZs and aerosols account for 13.8 % and 33.5 % of ALC profiles, respectively, compared to just 2.2% and 21.9% from CALIOP. These differences arise not only from the previously mentioned methodological factors such as the strict filtering criteria, but also from the local climate and microclimate at each site. The TZ layers detected by CALIOP were further classified as cirrus fringes (being present in 4.4% of all CALIOP profiles), Cluster 1 (1.4%; corresponding to features with optical properties between high-altitude ice clouds and aerosols at high altitudes, such as wispy cloud fragments) and Cluster 2 (2.7%; corresponding to features with optical properties between water clouds at low altitudes, such as hydrated aerosols).

In the present study, results show that TZ (also the case for clouds and aerosols) detected distributions are the combination of two sets, where some TZ layers are detected by both methods, others are only detected by one of the methods, and perhaps some layers are not being detected by any of the methods. Ground-based ALC observations offer high temporal and spatial resolution and are particularly useful for detecting TZ conditions at low altitudes, such as those associated with the top of the PBL, or with the formation and dissipation of shallow clouds. However, this method cannot cover large land or ocean areas, and the reduced sensitivity to optically thin, high-altitude layers, due to signal attenuation by height, resulted in an underestimation of TZ conditions at higher altitudes (e.g., cirrus fringes). In contrast, CALIOP provides global coverage and a comprehensive view of the vertical distribution of atmospheric layers. This method is especially useful to detect TZ conditions at high altitudes, such as cirrus fringes and Cluster 1 layers. Nevertheless, its coarser spatial resolution and the application of strict filters, lead to an underestimation of TZ layers at lower altitudes (e.g., Cluster 2). In addition, the CAD-score algorithm is biased towards classifying uncertain features as cloud in order to avoid cloud contamination in aerosol retrievals. As a consequence, a significant fraction of TZ layers is likely classified as clouds in the CALIOP products, consistent with previous findings (Fuchs and Cermak et al., 2015; Winker et al., 2009). Even though both lidars are capable of detecting multiple atmospheric layers within the same profile, attenuation by optically thick layers remains the main limitation for both methodologies. This laser attenuation by distance leads to an underestimation of TZ occurrence above (or below for CALIOP) dense cloud layers.

These findings are consistent with previous studies validating satellite retrievals with ground-based lidar (e.g., Kim et al., 2008; 2014; Perrone et al., 2011), and with studies studying TZ frequency of occurrence and spatial distribution (Fuchs et al., 2015; Marshak et al., 2011; Yu et al., 2026). To our knowledge, this is the first study to compare ALC retrievals (such as the CL51, CL31 and CT25K) with CALIOP, to assess diurnal and nocturnal TZ variations from CALIOP observations, and to present case studies of coincidental observations at small distances between the ground-based site and the satellite ground-track, varying from 0.10 to 3.67 km.

Despite the limitations stated, the synergy between both methods improves the description of the vertical structure, thickness, and occurrence of atmospheric layers. This integrated perspective is particularly

https://doi.org/10.5194/egusphere-2026-3737
Preprint. Discussion started: 28 August 2026

relevant for advancing the understanding of cloud-aerosol transition zones and their role in the atmosphere. Future work of our project aims to integrate other TZ observational methods (such as sky cameras, pyrgeometers and radiometers), to evaluate TZ representation in atmospheric models, with the final objective of reducing uncertainties associated with aerosol-cloud interactions and their radiative effects.

Appendix A

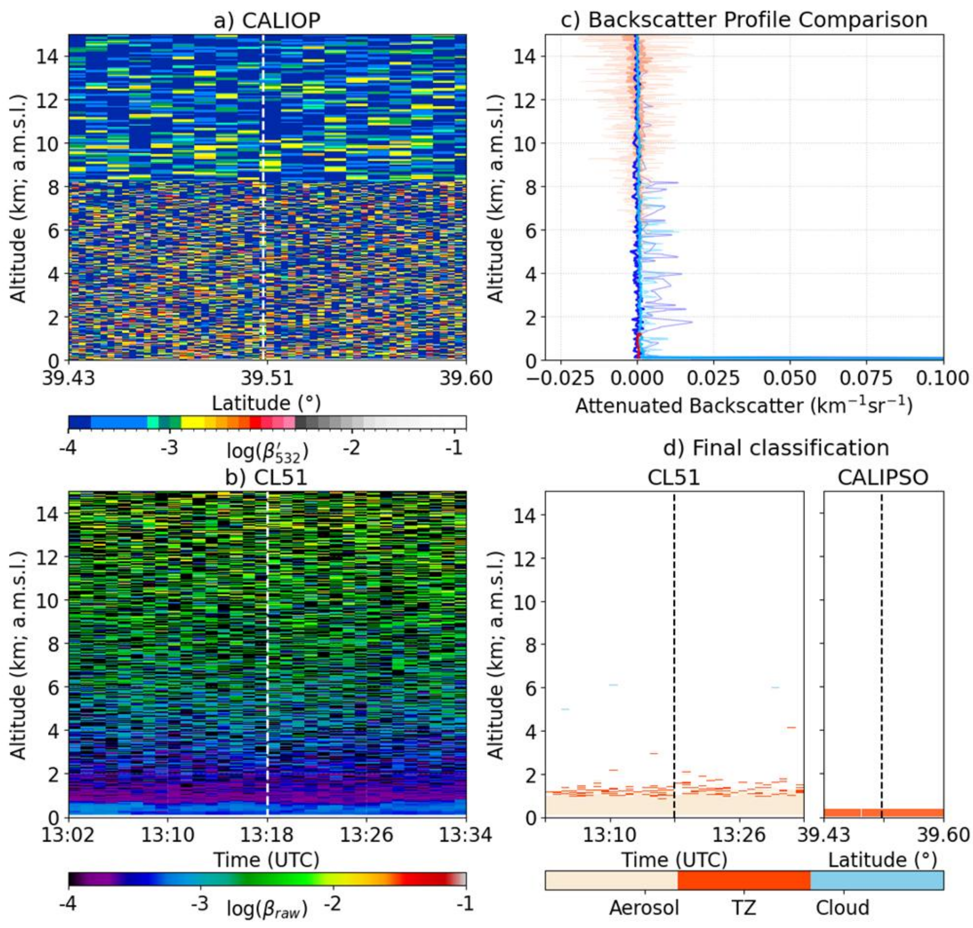

Figure A1: Same as Fig. 4 (cloud-free and PBL aerosols), but for the daytime case in (05/01/2017) at the BUR CL51 site. The CALIOP 532 nm attenuated backscatter coefficient spans 39.42 - 39.59º N, while raw-backscattered is from 13:02 to 13:34 UTC.

https://doi.org/10.5194/egusphere-2026-3737
Preprint. Discussion started: 28 August 2026

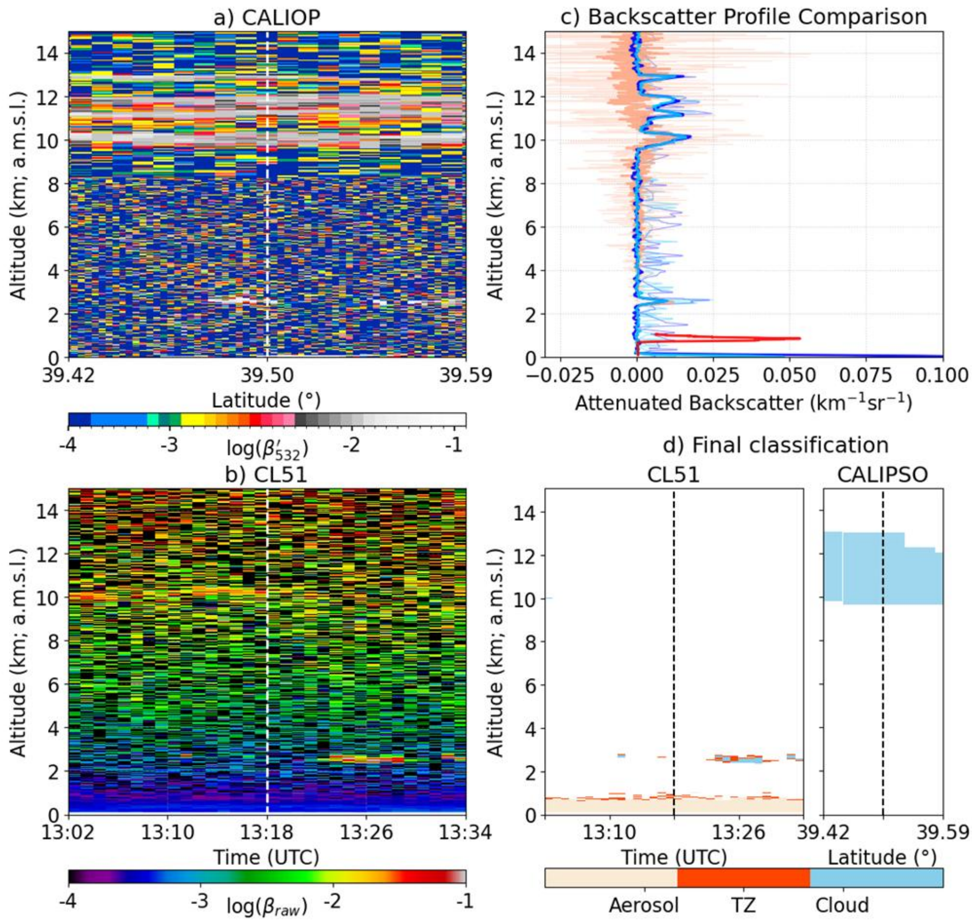

730 **Figure A2: Same as Fig. 4, but for cirrus clouds on 06/02/2017 over BUR. The CALIOP 532 nm attenuated backscatter coefficient spans 39.42 - 39.59º N, and raw-backscattered is from 13:02 to 13:34 UTC.**

https://doi.org/10.5194/egusphere-2026-3737
Preprint. Discussion started: 28 August 2026

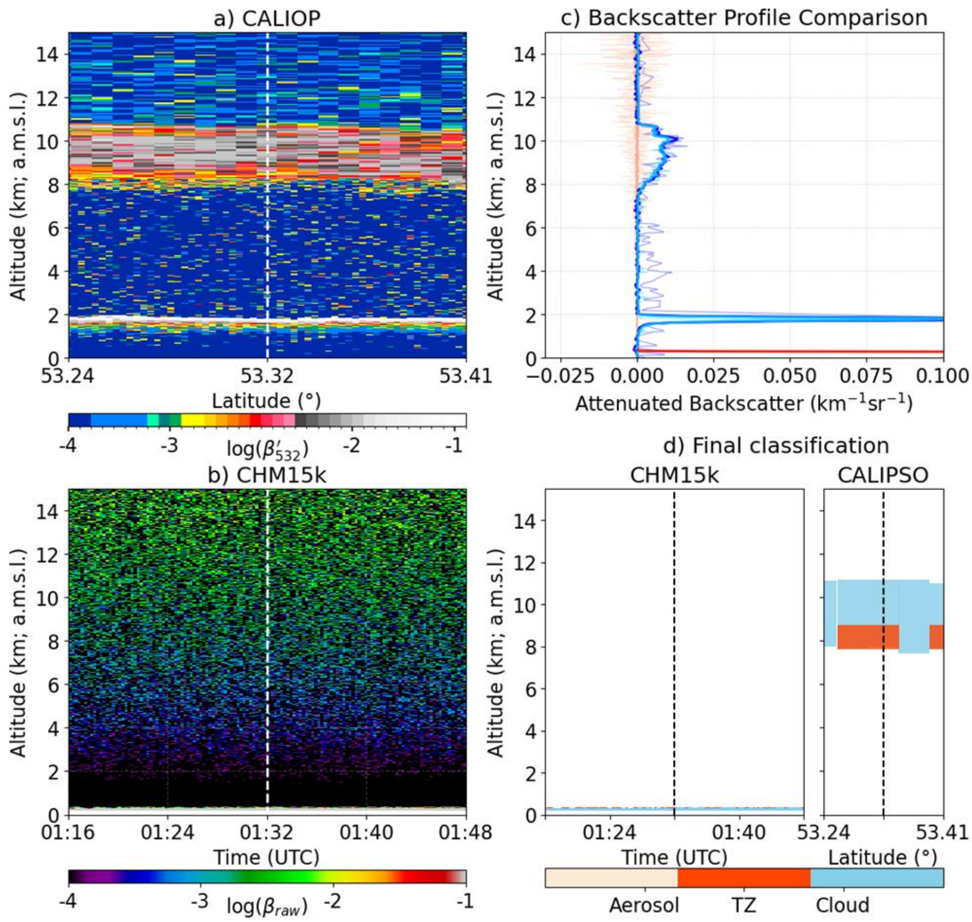

Figure A3: Same as Fig. 4, but for dense tropospheric clouds on 24/09/2017 over GRW. The CALIOP 532 nm attenuated backscatter coefficient spans 53.24 - 53.41º N, while raw-backscattered is from 01:16 to 01:48 UTC.

Appendix B

Table B1 Column integrated feature frequency (CI-FF, in %) detection for each of the ground-based ALC and CALIOP in 5º grid

		CALIOP						ALC		
Station code	Grid	Clouds	Total TZ	Cirrus fringes	Cluster 1	Cluster 2	Aerosols	Clouds	Total TZ	Aerosols
NYA	75–80º N, 10–15º E	76.6	8.8	4.9	1.2	3.0	20.3	64.3	73.8	99.8
KEN	65–70º N, 20–25º E	68.0	8.6	5.4	1.4	2.3	18.4	76.6	60.2	78.9
NOR	60–65º N, 15–20º E	64.3	7.0	3.8	1.3	2.3	20.8	68.7	70.8	99.5
GRW	50–55º N, 10–15º E	64.8	10.0	5.9	2.2	2.4	34.6	65.7	68.2	96.4
LIN	50–55º N, 10–15º E	64.8	10.0	5.9	2.2	2.4	34.6	66.0	75.0	95.3
CHB	50–55º N, -5–0º E	68.6	9.8	6.0	2.1	2.0	29.0	66.0	71.4	99.6
JUL	50–55º N, 5–10º E	64.7	8.6	5.1	1.9	2.0	32.3	61.6	73.2	98.9
PAL	45–50º N, 0–5º E	61.7	7.5	4.1	1.8	1.8	34.0	62.1	81.9	96.2
MUN	45–50º N, 10–15º E	55.9	6.5	3.5	1.3	1.9	32.5	56.0	60.4	97.3
SFH	45–50º N, 10–15º E	55.9	6.5	3.5	1.3	1.9	32.5	58.1	57.3	97.3
GIR	40–45º N, -5–0º E	46.9	6.5	2.9	1.6	2.3	37.5	26.1	23.1	98.9
BUR	35–40º N, -5–0º E	34.4	7.1	2.5	1.2	3.7	52.7	26.1	36.1	100.0

https://doi.org/10.5194/egusphere-2026-3737
Preprint. Discussion started: 28 August 2026

GRA	35–40º N, -5–0º E	34.4	7.1	2.5	1.2	3.7	52.7	25.0	56.3	98.9
LIM	30–35º N, 30–35º E	22.3	6.4	1.8	0.8	4.0	75.5	15.0	30.2	99.8
Total Europe	30–80º N, -10–35º E	60.0	8.2	4.4	1.4	2.7	34.6	52.7	59.9	96.9

Table B2 Column integrated hierarchical frequency (CI-HF, in %) detection for each ALC and CALIOP in 5º grid

	CALIOP			ALC		
Station code	Clouds	Total TZ	Aerosols	Clouds	Total TZ	Aerosols
NYA	76.6	1.6	7.0	64.3	10.2	25.5
KEN	68.0	1.2	8.1	76.6	8.8	14.6
NOR	64.3	1.9	10.9	68.7	4.3	27.0
GRW	64.8	2.6	18.4	65.7	9.7	24.6
LIN	64.8	2.6	18.4	66.0	14.0	20.0
CHB	68.6	1.9	15.8	66.0	7.1	26.9
JUL	64.7	2.1	18.1	61.6	15.0	23.4
PAL	61.7	2.0	20.2	62.1	24.9	13.0
MUN	55.9	1.6	21.1	56.0	12.5	31.5
SFH	55.9	1.6	21.1	58.1	15.5	26.4
GIR	46.9	2.4	24.9	26.1	7.3	66.6
BUR	34.4	3.8	39.5	26.1	10.6	63.3
GRA	34.4	3.8	39.5	25.0	33.4	41.6
LIM	22.3	4.2	64.8	15.0	20.2	64.8
Mean Europe	60.0	2.2	21.9	52.7	13.8	33.5

https://doi.org/10.5194/egusphere-2026-3737
Preprint. Discussion started: 28 August 2026

Appendix C

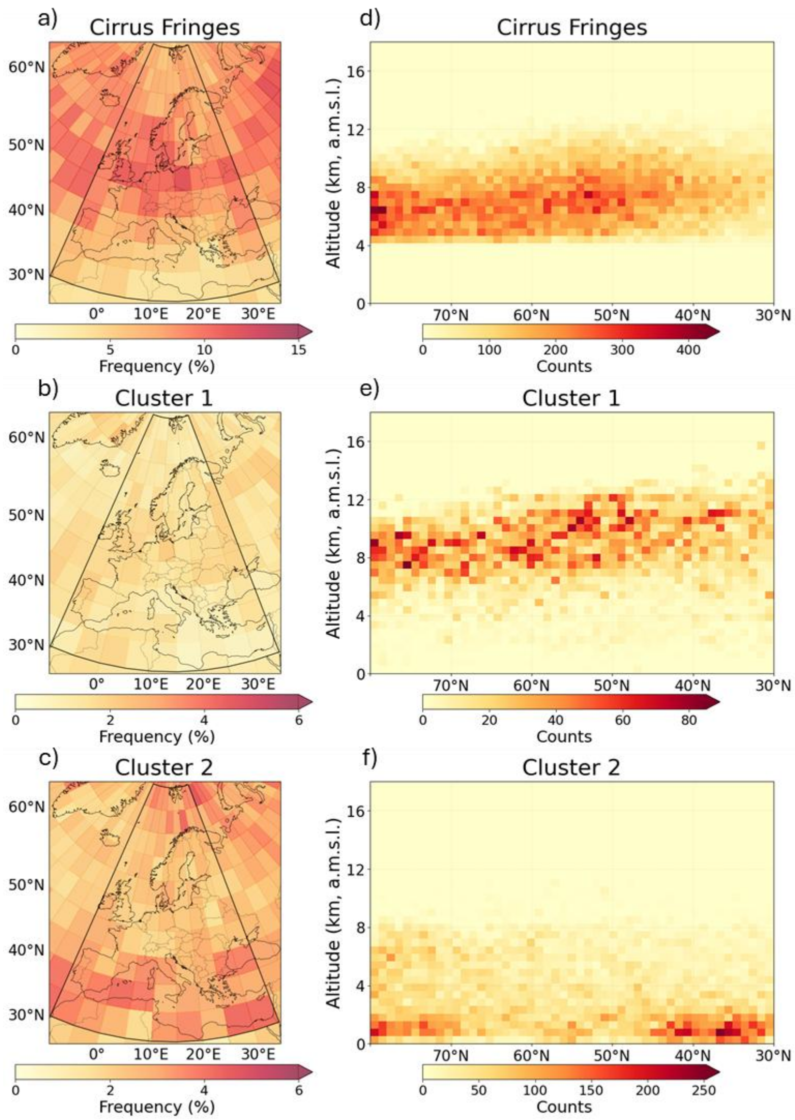

Figure C1: Transition zone subtypes distribution over Europe. a) Spatial distribution of the column integrated feature frequency (CI-FF) of cirrus fringes at 5º grid resolution; b) same as (a) but for Cluster 1; c) same as (a) but for Cluster 2; d) Vertical frequency of occurrence of cirrus fringes with 1º resolution on the x-axis, and 0.5 km on the y-axis; e) same as (d) but for Cluster 1; f) same as (d) but for Cluster 2.

Code and data availability

The GRW CHM15k data was provided by Deutscher Wetterdienst (DWD), the BUR CL51 was provided by the "Departament de Física de la Terra i Termodinàmica of the Universitat de València, and the GIR CL31 data by the "Departament de Física" of the Universitat de Girona. All this data is available at reasonable request. The Cloudnet ALC data was generated by ACTRIS and is available for download from https://cloudnet.fmi.fi. The ALC data was processed using the open-source Cloudnetpy algorithm (Tukiainen et al., 2020) available at https://github.com/actris-cloudnet/cloudnetpy.

The CALIPSO data was obtained from the NASA Langley Research Center Atmospheric Science Data Center (ASDC) available from https://asdc.larc.nasa.gov/: V4.51 CALIOP level 1B (https://doi.org/10.5067/CALIOP/CALIPSO/CAL_LID_L1-Standard-V4-51); and V.51 CALIOP level 2 merged layers (https://doi.org/10.5067/CALIOP/CALIPSO/CAL_LID_L2_05kmMLay-Standard-V4-51).

Author contribution

JRM conducted the research work and lead the writing of the main manuscript. JC and JAG supervised, acquired the funding and administrated the project. JLGA provided the BUR CL51 data. All authors contributed to the investigation, discussion, refinement of the results, and improvements of the paper.

Competing interest

The authors declare that they have no conflict of interest.

Acknowledgements

We would like to thank Ina Mattis and Frank Wagner from DWD for providing the GRW CHM15k data. We acknowledge ACTRIS and Finnish Meteorological Institute for providing the Cloudnet data which is available for download from https://cloudnet.fmi.fi. We also thank the CALIPSO science team for their efforts generating the CALIOP data. This study has been founded through project NUBOLOSYTI (PID2023-149972NB-100) of the Spanish Ministry of Science and Innovation (MICINN). JRM is supported by an IF-UdG 2022 fellowship, and JLGA is supported by the Spanish Research Agency, through the PELICAN project (PID2021-123881OB-I00).

References

Albrecht, B. A.: Aerosols, Cloud Microphysics, and Fractional Cloudiness. Sci., 245, 1227–1230, https://doi.org/10.1126/SCIENCE.245.4923.1227, 1989.

Alizadeh, O.: Advances and challenges in climate modeling. Clim. Change., 170, 1–26, https://doi.org/10.1007/S10584-021-03298-4, 2022.

Baroni, T., Pandey, P., Preissler, J., Gimmestad, G., and O'Dowd, C.: Comparison of Backscatter Coefficient at 1064 nm from CALIPSO and Ground–Based Ceilometers over Coastal and Non–Coastal Regions. Atmos., 11, 1190, https://doi.org/10.3390/ATMOS11111190, 2020.

Barthlott, C., Hoose, C., Barthlott, C., and Hoose, C.: Aerosol Effects on Clouds and Precipitation over Central Europe in Different Weather Regimes. J. Atmos. Sci., 75, 4247–4264, https://doi.org/10.1175/JAS-D-18-0110.1, 2018.

Boucher, O., Randall, D., Artaxo, P., Bretherton, C., Feingold, G., Forster, P., Kerminen, V.-M., Kondo, Y., Liao, H., Lohmann, U., Rasch, P., Satheesh, S.K., Sherwood, S., Stevens B., and Zhang, X.Y.: Clouds and Aerosols. In: Climate Change 2013: The Physical Science Basis. Contribution of Working Group I to the Fifth Assessment Report of the Intergovernmental Panel on Climate Change. Cambridge University Press, Cambridge, United Kingdom and New York, NY, USA. https://doi.org/10.1017/CBO9781107415324.016, 2013.

Bellini, A., Diémoz, H., di Liberto, L., Gobbi, G. P., Bracci, A., Pasqualini, F., and Barnaba, F.: ALICENET-an Italian network of automated lidar ceilometers for four-dimensional aerosol monitoring: Infrastructure, data processing, and applications. Atmos. Meas. Tech., 17, 6119–6144, https://doi.org/10.5194/AMT-17-6119-2024, 2024.

Cairo, F., di Liberto, L., Dionisi, D., and Snels, M.: Understanding Aerosol–Cloud Interactions through Lidar Techniques: A Review. Remote Sens., 16, 2788, https://doi.org/10.3390/RS16152788, 2024.

Calbó, J., Long, C. N., González, J. A., Augustine, J., and McComiskey, A.: The thin border between cloud and aerosol: Sensitivity of several ground based observation techniques. Atmos. Res., 196, 248–260, https://doi.org/10.1016/j.atmosres.2017.06.010, 2024.

Calbó, J., González, J.-A., Jahani, B., Sola, Y., and Ruiz de Morales, J.: How important is the transition zone between clouds and aerosol? AIP Conf. Proc., 2988, 070005, https://doi.org/10.1063/5.0182769, 2024.

Cazorla, A., Andrés Casquero-Vera, J., Román, R., Luis Guerrero-Rascado, J., Toledano, C., Cachorro, V. E., Orza, J. A. G., Cancillo, M. L., Serrano, A., Titos, G., Pandolfi, M., Alastuey, A., Hanrieder, N., and Alados-Arboledas, L.: Near-real-time processing of a ceilometer network assisted with sun-photometer data: Monitoring a dust outbreak over the Iberian Peninsula. Atmos. Chem. Phys., 17, 11861–11876, https://doi.org/10.5194/acp-17-11861-2017, 2017.

Ceppi, P., Brient, F., Zelinka, M. D., and Hartmann, D. L.: Cloud feedback mechanisms and their representation in global climate models. Wiley Interdisciplinary Rev. Clim. Change., 8, e465, https://doi.org/10.1002/wcc.465, 2017.

Chen, Y., Haywood, J., Wang, Y., Malavelle, F., Jordan, G., Peace, A., Partridge, D. G., Cho, N., Oreopoulos, L., Grosvenor, D., Field, P., Allan, R. P., and Lohmann, U.: Substantial cooling effect from aerosol-induced increase in tropical marine cloud cover. Nat. Geosci., 17, 404–410, https://doi.org/10.1038/S41561-024-01427-Z, 2024.

Chen, J., Zeng, X., Li, S., Song, G., and Li, S.: Water Vapor Correction in Measurements of Aerosol Backscatter Coefficients Using a 910 nm Vaisala CL51 Ceilometer. Remote Sens., 17, 12. https://doi.org/10.3390/RS17122013, 2025.

Deng, X., Xie, C., Liu, D., and Wang, Y.: Comparisons of aerosol types and optical characters over Shouxian Area China observed from ground- and space-based systems. Opt. Express., 32, 27081–27098, https://doi.org/10.1364/OE.524152, 2024a.

Deng, X., Xie, C., Liu, D., Wang, B., Xing, K., Chen, J., Ji, J., and Wang, Y.: Characteristics and seasonal variations of cirrus clouds from ground-based lidar and satellite observations over Shouxian Area, China. Opt. Express., 32, 21102–21120, https://doi.org/10.1364/OE.523574, 2024b.

Elias, T., Haeffelin, M., Drobinski, P., Gomes, L., Rangognio, J., Bergot, T., Chazette, P., Raut, J. C., and Colomb, M.: Particulate contribution to extinction of visible radiation: Pollution, haze, and fog. Atmos. Res., 92, 443–454, https://doi.org/10.1016/j.atmosres.2009.01.006, 2009.

Eytan, E., Gristey, J. J., and Feingold, G.: The Net Radiative Effect of the Ill-Defined Clear-Sky in the Vicinity of Clouds. AGU Adv., 6. https://doi.org/10.1029/2024AV001407, 2025.

Eytan, E., Koren, I., Altaratz, O., Kostinski, A. B., and Ronen, A.: Longwave radiative effect of the cloud twilight zone. Nat. Geosci., 13, 669–673, https://doi.org/10.1038/s41561-020-0636-8, 2020.

Fang, Z., Yang, H., Li, C., Kuang, Z., Xu, X., and Jin, H.: Reveal persistent haze pollution episodes in Hefei: a perspective from ground-based and satellite observation. Air Qual. Atmos. Health., 17, 2555–2568, https://doi.org/10.1007/s11869-024-01587-2, 2024.

Fuchs, J., and Cermak, J.: Where Aerosols become clouds-potential for global analysis based on CALIPSO data. Remote Sens., 7, 4178–4190, https://doi.org/10.3390/RS70404178, 2015.

Ghan, S., Wang, M., Zhang, S., Ferrachat, S., Gettelman, A., Griesfeller, J., Kipling, Z., Lohmann, U., Morrison, H., Neubauer, D., Partridge, D. G., Stier, P., Takemura, T., Wang, H., and Zhang, K.: Challenges in constraining anthropogenic aerosol effects on cloud radiative forcing using present-day spatiotemporal variability. Proc. Natl. Acad. Sci. U. S. A., 113, 5804–5811, https://doi.org/10.1073/PNAS.1514036113, 2016.

Gong, X., Wang, Y., Xie, H., Zhang, J., Lu, Z., Wood, R., Stratmann, F., Wex, H., Liu, X., and Wang, J.: Maximum Supersaturation in the Marine Boundary Layer Clouds Over the North Atlantic. AGU Adv., 4, e2022AV000855. https://doi.org/10.1029/2022AV000855

González, J. A., Calbó, J., and Sola, Y.: Assessment of cloudless-to-cloud transition zone from downwelling longwave irradiance measurements. Atmos. Res., 285, 106657, https://doi.org/10.1016/J.ATMOSRES.2023.106657, 2023.

Gu, J. F., Plant, R. S., Holloway, C. E., and Clark, P. A. The moist halo region around shallow cumulus clouds in large eddy simulations. Q. J. R. Meteorolog. Soc., 150, 1501–1517, https://doi.org/10.1002/QJ.4656, 2024.

Guerrero-Rascado, J. L., Landulfo, E., Antuña, J. C., de Melo Jorge Barbosa, H., Barja, B., Bastidas, Á. E., Bedoya, A. E., da Costa, R. F., Estevan, R., Forno, R., Gouveia, D. A., Jiménez, C., Larroza, E. G., da Silva Lopes, F. J., Montilla-Rosero, E., de Arruda Moreira, G., Nakaema, W. M., Nisperuza, D., Alegria, D., Múnera, M., Otero, L., Papandrea, S., Pallota, J.V., Pawelko, E., Quel, E. J., Ristori, P., Rodrigues, P. F., Salvador, J., Sánchez, M. F., and Silva, A.: Latin American Lidar Network (LALINET) for aerosol research: Diagnosis on network instrumentation. J. Atmos. S. Terr. Phys., 138–139, 112–120, https://doi.org/10.1016/J.JASTP.2016.01.001, 2016.

Haeffelin, M., Laffineur, Q., Bravo-Aranda, J.-A., Drouin, M.-A., Casquero-Vera, J.-A., Dupont, J.-C., and de Backer, H.: Radiation fog formation alerts using attenuated backscatter power from automatic lidars and ceilometers. Atmos. Meas. Tech., 9, 5347–5365, https://doi.org/10.5194/amt-9-5347-2016, 2016.

Harrison, R.G., Nicoll, K.A., Marlton, G.J., Ryder, C.L., and Bennett, A.J.: Saharan dust plume charging observed over the UK. Environ. Res. Lett., 13, 054018, https://doi.org/10.1088/1748-9326/AABCD9, 2018.

Hu, R., Li, Z., and Su, T.: Investigating Aerosol Hygroscopicity in the Subcloud Transition Zone and at the Surface in the Southern Great Plains. J. Geophys. Res.: Atmos., 130, e2024JD041925, https://doi.org/10.1029/2024JD041925, 2025.

Hunt, W. H., Vaughan, M. A., Powell, K. A., and Weimer, C.: CALIPSO Lidar Description and Performance Assessment. J. Atmos. Oceanic Technol., 26, 1214–1228, https://doi.org/10.1175/2009JTECHA1223.1, 2009.

Jahani, B., Calbó, J., and González, J. A. and Quantifying Transition Zone Radiative Effects in Longwave Radiation Parameterizations. Geophys. Res. Lett., 47, https://doi.org/10.1029/2020GL090408, 2020.

Jahani, B., Andersen, H., Calbo, J., Gonzalez, J. A., and Cermak, J.: Longwave radiative effect of the cloud-aerosol transition zone based on CERES observations. Atmos. Chem. Phys., 22, 1483–1494, https://doi.org/10.5194/ACP-22-1483-2022, 2022.

Kahn, R. A., Andrews, E., Brock, C. A., Chin, M., Feingold, G., Gettelman, A., Levy, R. C., Murphy, D. M., Nenes, A., Pierce, J. R., Popp, T., Redemann, J., Sayer, A. M., da Silva, A. M., Sogacheva, L., and Stier, P.: Reducing Aerosol Forcing Uncertainty by Combining Models With Satellite and Within-The-Atmosphere Observations: A Three-Way Street. Rev. Geophys., 61, e2022RG000796, https://doi.org/10.1029/2022RG000796, 2023.

https://doi.org/10.5194/egusphere-2026-3737
Preprint. Discussion started: 28 August 2026

Kim, S. W., Berthier, S., Raut, J. C., Chazette, P., Dulac, F., and Yoon, S. C.: Validation of aerosol and cloud layer structures from the space-borne lidar CALIOP using a ground-based lidar in Seoul, Korea. Atmos. Chem. Phys., 8, 3705–3720, https://doi.org/10.5194/ACP-8-3705-2008, 2008.

Kim, S. W., Chung, E. S., Yoon, S. C., Sohn, B. J., and Sugimoto, N.: Intercomparisons of cloud-top and cloud-base heights from ground-based Lidar, CloudSat and CALIPSO measurements. Int. J. Remote Sens., 32, 1179–1197, https://doi.org/10.1080/01431160903527439, 2011.

Kim, Y., Kim, S. W., Kim, M. H., and Yoon, S. C.: Geometric and optical properties of cirrus clouds inferred from three-year ground-based lidar and CALIOP measurements over Seoul, Korea. Atmos. Res., 139, 27–35, https://doi.org/10.1016/J.ATMOSRES.2013.12.016, 2014.

Kim, M. H., Yeo, H., Park, S., Park, D. H., Omar, A., Nishizawa, T., Shimizu, A., and Kim, S. W.: Assessing CALIOP-Derived Planetary Boundary Layer Height Using Ground-Based Lidar. Remote Sens., 13, 1496, https://doi.org/10.3390/RS13081496, 2021.

Koren, I., Remer, L. a., Kaufman, Y. J., Rudich, Y., and Martins, J. V.: On the twilight zone between clouds and aerosols. Geophys. Res. Lett., 34, 1–5, https://doi.org/10.1029/2007GL029253, 2007.

Kotthaus, S., O'Connor, E., Münkel, C., Charlton-Perez, C., Haeffelin, M., Gabey, A. M., and Grimmond, C. S. B.: Recommendations for processing atmospheric attenuated backscatter profiles from Vaisala CL31 ceilometers. Atmos. Meas. Tech., *9*, 3769–3791. https://doi.org/10.5194/AMT-9-3769-2016, 2016.

Kotthaus, S., and Grimmond, C.S.B.: Atmospheric boundary-layer characteristics from ceilometer measurements. Part 1: A new method to track mixed layer height and classify clouds. Quart. J. R. Meteorol. Soc., 144, 1525–1538, https://doi.org/10.1002/QJ.3299, 2018.

Kotthaus, S., Haeffelin, M., Drouin, M.A., Dupont, J.C., Grimmond, S., Haefele, A., Hervo, M., Poltera, and Y., Wiegner, M.: Tailored algorithms for the detection of the atmospheric boundary layer height from common automatic lidars and ceilometers (ALC). Remote Sens., 12, 3259, https://doi.org/10.3390/rs12193259, 2020.

Li, D., Wu, Y., Gross, B., and Moshary, F.: Capabilities of an Automatic Lidar Ceilometer to Retrieve Aerosol Characteristics within the Planetary Boundary Layer. Remote Sens., 13, 3626, https://doi.org/10.3390/RS13183626, 2021.

Malik, D., Andersen, H., Cermak, J., Vogt, R., and Adler, B.: Cloud Base Height Determines Fog Occurrence Patterns in the Namib Desert and Can Be Estimated from Near-Surface Relative Humidity, [preprint], https://doi.org/10.5194/EGUSPHERE-2025-2645, 2025.

Mamouri, R. E., Amiridis, V., Papayannis, A., Giannakaki, E., Tsaknakis, G., and Balis, D. S.: Validation of CALIPSO space-borne-derived attenuated backscatter coefficient profiles using a ground-based lidar in Athens, Greece. Atmos. Meas. Tech., 2, 513–522, https://doi.org/10.5194/AMT-2-513-2009, 2009.

Marcos, C. R., Pedrós, R., Gómez-Amo, J. L., Utrillas, M. P., and Martínez-Lozano, J. A.: Analysis of Desert Dust Outbreaks Over Southern Europe Using CALIOP Data and Ground-Based Measurements. IEEE Trans. Geosci. Remote Sens., 54, 744–756, https://doi.org/10.1109/TGRS.2015.2464701, 2016.

Masson-Delmotte, V., P. Zhai, A. Pirani, S.L. Connors, and Coauthors.: IPCC, 2021: Climate Change 2021: The Physical Science Basis. Contribution of Working Group I to the Sixth Assessment Report of the Intergovernmental Panel on Climate Change. Camb. Univ. Press, Cambridge, United Kingdom and New York, NY, USA, https://doi.org/10.1017/9781009157896, 2021.

Nishizawa, T., Sugimoto, N., Matsui, I., Shimizu, A., Higurashi, A., and Jin, Y.: The Asian Dust and Aerosol Lidar Observation Network (AD-NET): Strategy and Progress. EPJ Web Conf., 119, 19001, https://doi.org/10.1051/EPJCONF/201611919001, 2016.

https://doi.org/10.5194/egusphere-2026-3737
Preprint. Discussion started: 28 August 2026

Pappalardo, G., Wandinger, U., Mona, L., Hiebsch, A., Mattis, I., Amodeo, A., Ansmann, A., Seifert, P., Linné, H., Apituley, A., Arboledas, L. A., Balis, D., Chaikovsky, A., D'Amico, G., de Tomasi, F., Freudenthaler, V., Giannakaki, E., Giunta, A., Grigorov, I., Iarlori, M., Madonna, F., Mamouri, R.E., Nasti, L., Papayannis, A., Pietruczuk, A., Pujades, M., Rizi, V., Rocadenbosch, F., Russo, F., Schnell, F., Spinelli, N., Wang, X., and Wiegner, M.: EARLINET correlative measurements for CALIPSO: First intercomparison results. J. Geophys. Res. Atmos., 115. https://doi.org/10.1029/2009JD012147, 2010.

Pappalardo, G., Amodeo, A., Apituley, A., Comeron, A., Freudenthaler, V., Linné, H., Ansmann, A., Bösenberg, J., D'amico, G., Mattis, I., Mona, L., Wandinger, U., Amiridis, V., Alados-Arboledas, L., Nicolae, D., and Wiegner, M.: EARLINET: towards an advanced sustainable European aerosol lidar network. Atmos. Meas. Tech., 7, 2389–2409, https://doi.org/10.5194/amt-7-2389-2014, 2014.

Pauli, E., Cermak, J., and Andersen, H.: A satellite-based climatology of fog and low stratus formation and dissipation times in central Europe. Q. J. R. Meteorolog. Soc., 148, 1439–1454, https://doi.org/10.1002/qj.4272, 2022.

Perrone, M. R., de Tomasi, F., and Burlizzi, P.: Aerosol products by CALIOP at 532 nm and by a ground-based Raman lidar at 355 nm: Intercomparison methodology. Atmos. Res., 101, 438–449, https://doi.org/10.1016/J.ATMOSRES.2011.04.005, 2011.

Peshev, Z., Deleva, A., Vulkova, L., and Dreischuh, T.: Large-Scale Saharan Dust Episode in April 2019: Study of Desert Aerosol Loads over Sofia, Bulgaria, Using Remote Sensing, In Situ, and Modeling Resources. Atmos., 13, https://doi.org/10.3390/atmos13060981, 2022.

Qin, K., Wu, L., Wong, M. S., Letu, H., Hu, M., Lang, H., Sheng, S., Teng, J., Xiao, X., and Yuan, L.: Trans-boundary aerosol transport during a winter haze episode in China revealed by ground-based Lidar and CALIPSO satellite. Atmos. Environ., 141, 20–29, https://doi.org/10.1016/j.atmosenv.2016.06.042, 2016.

Rogers, R.R., Lamoureux, M.-F., Bissonnette, L.R., and Peters, R.M.: Quantitative interpretation of laser ceilometer intensity profiles. J. Atmos. Ocean. Technol., 14, 396–411. https://doi.org/10.1175/1520-0426(1997)014<0396:QIOLCI>2.0.CO;2, 1997.

Ronen, R., Koren, I., Levis, A., Eytan, E., Holodovsky, V., and Schechner, Y. Y.: 3D volumetric tomography of clouds using machine learning for climate analysis. Sci. Rep., 15(1), 1–12, https://doi.org/10.1038/S41598-025-90169-Y, 2025.

Ruiz de Morales, J., Calbó, J., González, J. A., and Sola, Y.: A method to assess the cloud-aerosol transition zone from ceilometer measurements. Atmos. Res., 310, 107623, https://doi.org/10.1016/J.ATMOSRES.2024.107623, 2024.

Ruiz de Morales, J., Calbó, J., González, J. A., Andersen, A., Cermak, J., Fuchs, J., and Sola, Y.: Global Assessment of the Cloud-Aerosol Transition Zone Using CALIPSO. Adv. Atmos. Sci., 43, 321–335, https://doi.org/10.1007/s00376-025-5052-y, 2026.

Scarlatti, F., Gómez-Amo, J. L., Valdelomar, P. C., Estellés, V., and Utrillas, M. P.: A Machine Learning Approach to Derive Aerosol Properties from All-Sky Camera Imagery. Remote Sens., 15, 1676, https://doi.org/10.3390/RS15061676, 2023.

Scarlatti, F., Gómez-Amo, J. L., Valdelomar, P. C., Estellés, V., and Utrillas, M. P.: An improved approach to determine aerosol properties from all-sky camera imagery: Sensitivity to the partially cloud scenes. Atmos. Environ., 327, 120495, https://doi.org/10.1016/J.ATMOSENV.2024.120495, 2024.

Segura, S., Estellés, V., Utrillas, M. P., and Martínez-Lozano, J. A.: Long term analysis of the columnar and surface aerosol relationship at an urban European coastal site. Atmos. Environ., 167, 309–322, https://doi.org/10.1016/j.atmosenv.2017.08.012, 2017.

https://doi.org/10.5194/egusphere-2026-3737
Preprint. Discussion started: 28 August 2026

Snels, M., Colao, F., Cairo, F., Shuli, I., Scoccione, A., de Muro, M., Pitts, M., Poole, L., and di Liberto, L.: Quasi-coincident observations of polar stratospheric clouds by ground-based lidar and CALIOP at Concordia (Dome C, Antarctica) from 2014 to 2018. Atmos. Chem. Phys., 21, 2165–2178, https://doi.org/10.5194/ACP-21-2165-2021, 2021.

Tukiainen, S., O'Connor, E., and Korpinen, A.: CloudnetPy: A Python package for processing cloud remote sensing data. J. Open Source Software., 5, 2123. https://doi.org/10.21105/JOSS.02123, 2020.

Twomey, S.: Pollution and the planetary albedo. Atmos. Environ., 8, 1251–1256, https://doi.org/10.1016/0004-6981(74)90004-3, 1974.

Twomey, S.: Aerosols, clouds and radiation. Atmos. Environ., 25, 2435–2442, https://doi.org/10.1016/0960-1686(91)90159-5, 1991.

Várnai, T., and Marshak, A.: Global CALIPSO Observations of Aerosol Changes Near Clouds. IEEE Geosci. Remote Sens. Lett., 8, 19–23, https://doi.org/10.1109/LGRS.2010.2049982, 2011.

Wang, S., Zhang, X., Zhang, D., Ren, G., Li, W., Xu, L., Wang, G., & Li, W.: The effect of continental aerosols on cloud-rain transition processes in winter based on aircraft observations. Atmos. Res., 314, 107749. https://doi.org/10.1016/J.ATMOSRES.2024.107749, 2025a.

Wang, Y., Neubauer, D., Chen, Y., Jordan, G., Malavelle, F., Yuan, T., Partridge, D., Field, P., Wang, H., Wang, M., Michou, M., Nabat, P., Laakso, A., Myhre, G., and Lohmann, U. Global climate models are unable to reproduce cloud cover response to aerosol, [preprint], https://doi.org/10.21203/RS.3.RS-6672054/V1, 2025b.

Welton, E. J., Stewart, S. A., Lewis, J. R., Belcher, L. R., Campbell, J. R., and Lolli, S.: Status of the NASA Micro Pulse Lidar Network (MPLNET): overview of the network and future plans, new version 3 data products, and the polarized MPL. EPJ Web Conf., 176, 09003, https://doi.org/10.1051/EPJCONF/201817609003, 2018.

Wen, G., and Marshak, A.: Precipitable Water Vapor Variation in the Clear-Cloud Transition Zone from the ARM Shortwave Spectrometer. IEEE Geosci. Remote Sens. Lett., 19, https://doi.org/10.1109/LGRS.2021.3064334, 2022.

Wen, G., Marshak, A., Levy, R., and Schuster, G.: Accounting for 3D radiative effects in MODIS aerosol retrievals near clouds using CALIPSO observations. Front. Remote Sens., 4, 1333814, https://doi.org/10.3389/frsen.2023.1333814, 2024.

Wendisch, M., Macke, A., Ehrlich, A., Lüpkes, C., Mech, M., Chechin, D., Dethloff, K., Velasco, C. B., Bozem, H., Brückner, M., Clemen, H.-C., Crewell, S., Donth, T., Dupuy, R., Ebell, K., Egerer, U., Engelmann, R., Engler, C., Eppers, O., Gehrmann, M., Gong, X., Gottschalk, M., Gourbeyre, C., Griesche, H., Hartmann, J., Hartmann, M., Heinold, B., Herber, A., Herrmann, H., Heygster, G., Hoor, P., Jafariserajehlou, S., Jäkel, E., Järvinen, E., Jourdan, O., Kästner, U., Kecorius, S., Knudsen, E. M., Köllner, F., Kretzschmar, J., Lelli, L., Delphine, L., Marturilli, M., Mei, L., Mertes, S., Mioche, G., Neuber, R., Nicolaus, M., Nomokonova, T., Notholt, J., Palm, M., van Pinxteren, M., Quaas, J., Richter, P., Ruiz-Donoso, E., Schäfer, M., Schmieder, K., Schnaiter, M., Schneifer, J., Schwarzenböck, A., Seifert, P., Schupe, M. D., Siebert, H., Spreen, G., Stapf, J., Stratmann, F., Vogl, T., Welti, A., Wex, H., Wiedenshler, A., Zanatta, M., and Zeppenfeld, S.: The Arctic Cloud Puzzle: Using ACLOUD/PASCAL Multiplatform Observations to Unravel the Role of Clouds and Aerosol Particles in Arctic Amplification. Bull. Am. Meteorol. Soc., 100, 841–871, https://doi.org/10.1175/BAMS-D-18-0072.1, 2019.

Wiegner, M., Madonna, F., Binietoglou, I., Forkel, R., Gasteiger, J., Geiß, A., Pappalardo, G., Schäfer, K., amd Thomas, W.: What is the benefit of ceilometers for aerosol remote sensing? An answer from EARLINET. Atmos. Meas. Tech., 7, 1997. https://doi.org/10.5194/AMT-7-1979-2014, 2014.

https://doi.org/10.5194/egusphere-2026-3737
Preprint. Discussion started: 28 August 2026

Winker, D. M., Pelon, J., Coakley, J. A., Ackerman, S. A., Charlson, R. J., Colarco, P. R., Flamant, P., Fu, Q., Hoff, R. M., Kittaka, C., Kubar, T. L., Treut, H. le, Mccormick, M. P., Mégie, G., Poole, L., Powell, K., Trepte, C., Vaughan, M. A., and Wielicki, B. A.: The CALIPSO Mission: A Global 3D View of Aerosols and Clouds. Bull. Am. Meteorol. Soc., 91, 1211–1230.,https://doi.org/10.1175/2010BAMS3009.1, 2010.

Yang, H., Fang, Z., Deng, X., Cao, Y., and Xie, C.: Detection by Space-Borne and Ground-Based Lidar Observations of Air Pollution on the Example of the Hefei Area. J. Appl. Spectrosc., 88, 1304–1314, https://doi.org/10.1007/S10812-022-01312-W, 2022.

Yang, F., Kostinski, A. B., Zhu, Z., Lamer, K., Luke, E., Kollias, P., Sua, Y. M., Hou, P., Shaw, R. A., and Vogelmann, A. M.: A single-photon lidar observes atmospheric clouds at decimeter scales: resolving droplet activation within cloud base. Npj Clim. Atmos. Sci., 7, 92, https://doi.org/10.1038/s41612-024-00644-y, 2024.

Yuba, A., Huo, M., and Sato, K.: Global Atmosphere Watch (GAW) Aerosol Program. Handbook of Air Quality and Climate Change, 1–29, https://doi.org/10.1007/978-981-15-2527-8_9-1, 2023.